Article

Current Biology

Gravity-dependent choice of frame of reference in the posterior parietal cortex

Graphical abstract

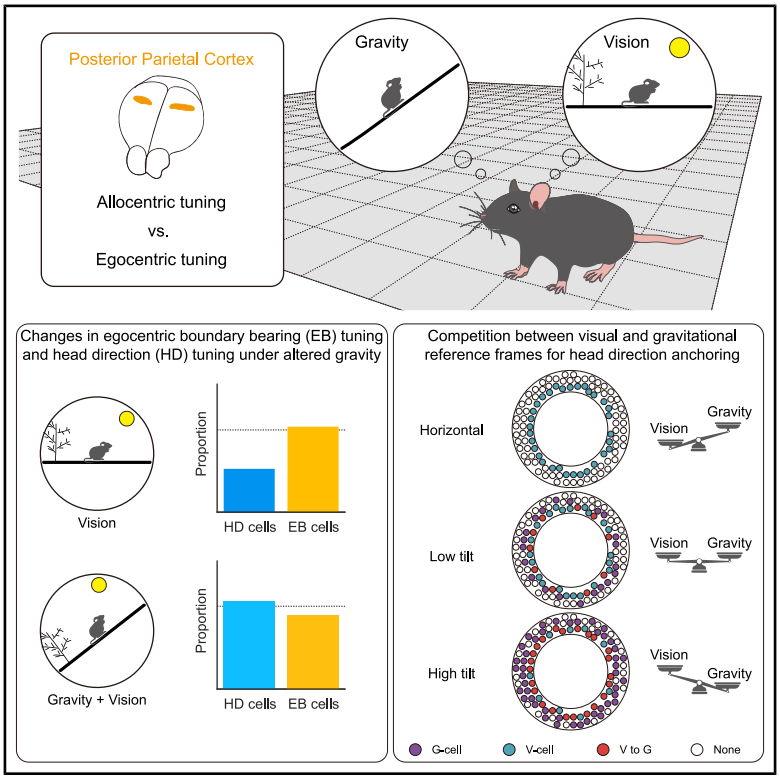

Highlights

- We studied head direction and egocentric boundary representations on tilted planes
- Head direction tuning is enhanced, and egocentric tuning is weakened on tilted planes
- Gravity-anchored head direction cells emerge on sloping terrain
- Competition exists between vision and gravity reference frames for head direction

Authors

Junyu Zhao, Baishun An, Ning Cheng, Qiqi Dong, Cheng Wang, Xiaojing Chen

Correspondence

cheng.wang1@siat.ac.cn (C.W.), chenxj@sustech.edu.cn (X.C.)

In brief

On tilted navigational planes, Zhao et al. demonstrate that the gravity signal enhances allocentric head direction representation while weakening egocentric boundary bearing tuning. Head direction cells anchored to gravity begin to dominate over visually controlled cells. The results suggest a flexible choice of reference frames by PPC cells.

Zhao et al., 2025, Current Biology *35*, 4882–4897
October 20, 2025 © 2025 Elsevier Inc. All rights are reserved, including those for text and data mining, AI training, and similar technologies.
https://doi.org/10.1016/j.cub.2025.08.048

CellPress

CellPress

Current Biology

Article

Gravity-dependent choice of frame of reference in the posterior parietal cortex

Junyu Zhao,[1,5] Baishun An,[1,5] Ning Cheng,[2,5] Qiqi Dong,[2] Cheng Wang,[2,3,4,*] and Xiaojing Chen[1,6,*]

[1]Brain Research Centre, Department of Neuroscience, School of Life Sciences, Southern University of Science and Technology, Shenzhen 518055, China

[2]Shenzhen Key Laboratory of Precision Diagnosis and Treatment of Depression, Shenzhen-Hong Kong Institute of Brain Science, Shenzhen Institutes of Advanced Technology, Chinese Academy of Sciences, Shenzhen 518055, China

[3]Guangdong Provincial Key Laboratory of Brain Connectome and Behavior, the Brain Cognition and Brain Disease Institute, Shenzhen Institutes of Advanced Technology, Chinese Academy of Sciences, Shenzhen 518055, China

[4]State Key Laboratory of Brain Cognition and Brain-inspired Intelligence Technology, Chinese Academy of Sciences, Shanghai 200031, China

[5]These authors contributed equally

[6]Lead contact

*Correspondence: cheng.wang1@siat.ac.cn (C.W.), chenxj@sustech.edu.cn (X.C.)

https://doi.org/10.1016/j.cub.2025.08.048

SUMMARY

Reference frame is an essential concept for spatial navigation. The principles underlying the choice of reference frames by neuronal ensembles, especially under natural conditions, which involve sloping terrains, remain unclear. The posterior parietal cortex (PPC) is a central region for navigation and movement control, and it contains several distinct types of reference frames. Here, we investigated the influence of gravity signals on egocentric tuning and allocentric head direction tuning in the mouse PPC by introducing a mismatch between visual input and gravitational signals by tilting the ground. We found that the allocentric head direction tuning and egocentric boundary bearing tuning were differentially controlled by altered gravity signals. Specifically, the allocentric head direction signals became stronger, whereas the egocentric boundary signal was weakened. However, across horizontal and tilted conditions, the head direction tuning was less consistent, as the head directional signal could be anchored to a visual or gravity frame of reference. As the mismatch between gravitational and visual inputs increased, the gravity-anchored head direction cells became dominant. Notably, individual head direction cells can switch between reference frames. Together, these results suggest that PPC neurons exhibit a highly flexible selection of reference frames based on task demands, which may allow efficient navigation strategies in natural environments.

INTRODUCTION

Navigation necessitates the use of spatial information of the self and external items, and this spatial information must be defined within a chosen frame of reference. Due to the diverse sensory inputs and action outputs, different types of frames of reference are employed.[1–8] Allocentric (world-centered) and egocentric (self-centered) frames of reference refer to the definition of spatial information with respect to the external world or to the self, respectively. Depending on the nature of the external reference, allocentric coordinates can be classified as either local/global frame of reference based on cue proximity[3] or visual/auditory frame of reference based on the sensory modality of the cues,[9] etc. Likewise, egocentric representations may be defined relative to the body, head, or eyes.[1] Despite these classifications, it remains unclear how a single brain region handles the use and transformation between different frames of reference across varied behavioral conditions.

The posterior parietal cortex (PPC) is crucial in the processing of spatial sensory information for motor action and navigation.[1,2,4,10–16] PPC neurons have been shown to encode egocentric information about self-motion[12,14,15,17,18] as well as external sensory stimuli, such as visual stimuli, environmental boundaries, and discrete objects.[1,4,7,13,15,19,20] Therefore, PPC is thought to be part of a network transforming egocentric representation to allocentric representation in the hippocampus-centered navigation system.[2,5,6,13,21,22] PPC neurons can also be sensitive to global allocentric information.[10,12,13,15,17,20,23] The exact relationship between egocentric representation and allocentric head direction (HD) signal in the PPC is still unknown, especially under more complex and natural navigation scenarios.

Animals on Earth have developed an inherent understanding of gravity as their behaviors and perceptions have evolved in response to Earth's gravitational pull. Thus, the influence of gravity is fundamental to our environmental awareness and plays a pivotal role in our ability to navigate. Moreover, the three-dimensional nature of the terrain topology requires 3D space perception and the proper use of efficient 3D navigation strategies. Although there are studies investigating the role of gravity on the spatial representations in the hippocampus and related navigation system,[24–36] not much is known about how gravitational input influences the choice of reference frames for representing spatial information.

Here, we explored the egocentric and allocentric representations in PPC with two sets of behavioral tasks: the sloping terrain

All rights are reserved, including those for text and data mining, AI training, and similar technologies.

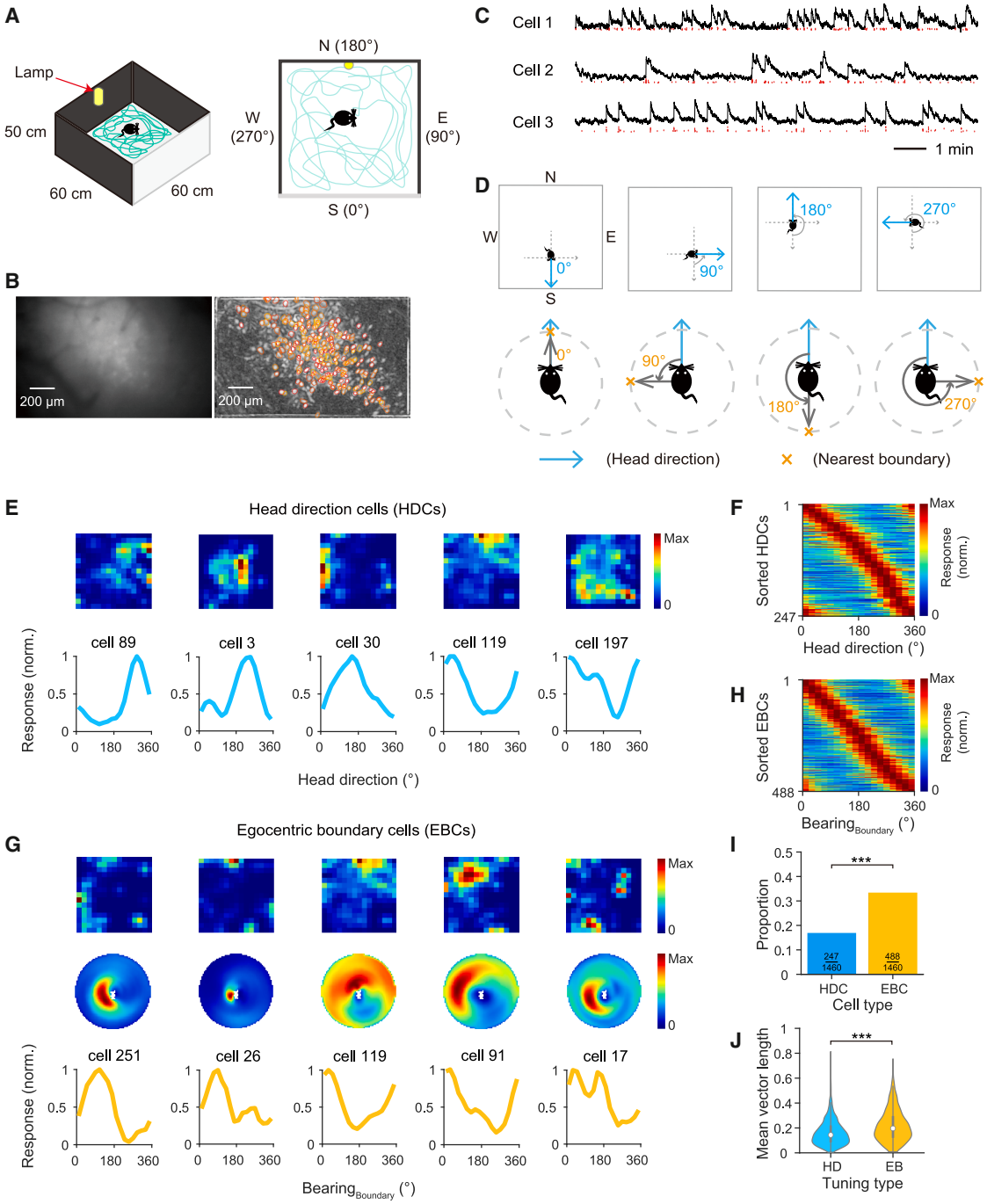

Figure 1. Egocentric boundary bearing tuning and head direction tuning of PPC neurons during horizontal open-field foraging task

(A) Schematics of the apparatus. The red arrow denotes the LED lamp.

(B) Left: a raw calcium fluorescence frame. Right: all recorded cells in the session with the contours denoting the extracted cells.

(C) Raw calcium traces (black lines) and deconvolved calcium events (red) for three example cells.

(D) Definitions of allocentric head direction (HD) and egocentric boundary bearing (EB).

(E) Example HD cells (HDCs). For each cell, (top) spatial rate map (red, peak response; blue, zero) and (bottom) HD tuning curve.

(F) Sorted HD tuning curves based on the direction of their peak responses.

(G) Example of egocentric boundary cells (EBCs). For each cell, (top) spatial rate map (red, peak response; blue, zero), (middle) egocentric boundary rate map (EBR), and (bottom) boundary bearing tuning curve.

(legend continued on next page)

task, which is an open-field-foraging task with different slopes of the locomotion plane, and the tilted virtual reality (VR) task. We found that the egocentric representation of environmental boundaries was weakened and that of visual landmarks was unaltered. However, the representation of allocentric HD was enhanced. We uncovered two types of HD cells (HDCs) that use visual or gravitational information as their frame of reference. With increasing slope, there was a gradual increase in gravity-anchored HDCs (G-cells) at the expense of vision-anchored HDCs (V-cells). These results demonstrated that gravity-centered allocentric representation dominates the activity of PPC neurons when visual input and gravitational input are in conflict.

RESULTS

Allocentric HD and egocentric boundary representations in the PPC

We recorded PPC neuron activity in eight mice using one-photon calcium imaging during a horizontal open-field-foraging task (Figures 1A–1C, S1A, and S1B; Table S1). A total of 1,460 cells were analyzed. The mice freely explored a square box, in which an LED light on the north wall served as the primary landmark (Figure 1A; STAR Methods). Cells were classified as egocentric boundary cells (EBCs) or HDCs if they passed the shuffling test and had a respective mean vector length (MVL) greater than 0.25. Conjunctive egocentric boundary bearing (EB) × HD cells met both criteria for EB and HD (STAR Methods). We analyzed allocentric HD and EB tuning for each neuron and detected 16.9% (247/1,460) of neurons as HDCs (Figures 1E, 1F, 1I, and S1C) and 33.4% (488/1,460) as EBCs (Figures 1G–1I, S1D, and S1E). We also identified 7.95% (116/1,460) of cells that showed conjunctive selectivity for HD and EB, significantly higher than expected by assuming HDCs and EBCs belong to independent populations of cells (Figure S1F). Thus, 23.77% of EBCs also showed conjunctive tuning for HD. In addition, the EBCs showed a wide range of distance selectivity, but most of them show animal-proximal distance preference (Figures S1G–S1I). Thus, the EBCs reported here are similar to those reported in Alexander et al.[37]

The proportion of EBCs was significantly higher than that of HDCs (Figure 1I; $\chi^2 = 105.60$, $p < 0.0001$). In addition, we found that both the tuning strength (measured by MVL) and tuning consistency across days were significantly higher for the EB representation than the HD representation (Figure 1J; Wilcoxon signed-rank test, $p = 8.29 \times 10^{-45}$; Figures S1J–S1N). Thus, overall, PPC neurons exhibit a stronger preference for the egocentric representation together with a mixed selectivity for allocentric HD.[2,5,13]

Influence of gravitational input on HD and egocentric boundary representation

We next examined the influence of gravitational input on the allocentric HD and egocentric boundary representations during the sloping terrain task, where the arena was tilted at angles of 0°, 20°, and 40° along the east-west axis with the floor oriented toward the east (Figure 2A; STAR Methods). We recorded 3,236 PPC cells from 6 mice over 3 sessions, and tracked 508 cells in all three sessions. Results showed that the tuning strength of the same individual cells varied across tilt conditions (Figures 2B and 2D).

We compared the proportions of HDCs and EBCs across different tilt conditions. The proportion of HDCs increased to 23.43% (119/508) at 20° tilt and 38.39% (195/508) at 40° tilt, compared with 17.52% (89/508) in the horizontal condition (Figures 2C and S2A; Cochran-Armitage trend test: $Z = 7.54$, $p = 4.69 \times 10^{-14}$; chi-squared post hoc tests: 0° vs. 20°, $p = 0.020$; 0° vs. 40°, $p = 1.26 \times 10^{-13}$; 20° vs. 40°, $p = 2.47 \times 10^{-7}$, using a Bonferroni-corrected significance threshold of $\alpha = 0.0167$). By contrast, the proportion of EBCs decreased to 32.09% (163/508) at 20° tilt and 32.87% (167/508) at 40° tilt, from 40.35% (205/508) in the horizontal condition (Figures 2E and S2B; Cochran-Armitage trend test: $Z = -2.50$, $p = 0.012$; chi-squared post hoc tests: 0° vs. 20°, $p = 0.0061$. 0° vs. 40°, $p = 0.013$. 20° vs. 40°, $p = 0.79$; using a Bonferroni-corrected significance threshold of $\alpha = 0.0167$). The conclusion holds true for individual mice, and similar results were drawn in the retrosplenial cortex (RSC) (Figures S2C and S2D).

We compared the MVL values between HD tuning and EB tuning (MVL_{HD} vs. MVL_{EB}) in each tilt condition for all recorded cells (Figure 2F). With increased tilt angles, the MVL_{HD} was increased, whereas the MVL_{EB} remained unchanged. We found EB tuning was significantly stronger than HD tuning in the horizontal or 20° tilt condition, but this dominance was reversed in 40° tilt condition (Figure 2F; Wilcoxon signed-rank tests, all cells, $n = 508$ cells: 0° tilt, $p = 7.56 \times 10^{-26}$, 20° tilt, $p = 7.50 \times 10^{-4}$, 40° tilt, $p = 0.0015$). Comparing HD tuning across tilt conditions, HD tuning strength increased with tilt angle (Figure S2E), while EB tuning weakened. We created a bias index to quantify the extent of allocentric vs. egocentric representation ($Bias\ Index = \frac{MVL_{EB} - MVL_{HD}}{MVL_{EB} + MVL_{HD}}$). The positive bias index indicates a preference for EB, while the negative bias index indicates a preference for HD. We found that the bias index decreased as the slope increased (Figure 2G; all cells, Friedman test, $p = 5.57 \times 10^{-23}$; Dunn's test for post hoc test: 0° vs. 20°, $p < 0.0001$. 0° vs. 40°, $p < 0.0001$. 20° vs. 40°, $p < 0.0001$; Wilcoxon rank-sum test for each subtype, using a Bonferroni-corrected significance threshold of $\alpha = 0.0167$, pure HDCs, 0° vs. 20°: $p = 0.25$, 0° vs. 40°: $p = 0.0086$, 20° vs. 40°: $p = 0.098$; pure EBCs, 0° vs. 20°: $p = 0.0051$, 0° vs. 40°: $p = 0.00071$, 20° vs. 40°: $p = 0.18$; conjunctive cells, 0° vs. 20°: $p = 0.30$, 0° vs. 40°: $p = 0.0015$, 20° vs. 40°: $p = 0.030$; Figures S2F–S2H). We also tracked the same cells across pairs of tilt conditions and found that the differences in MVL showed a clear trend of strengthened HD coding as conditions shifted from horizontal to tilted (Figure S2I). Moreover, we examined the

(H) Same as (F), but for EBCs.
(I) Histogram showing the proportions of HDCs (blue) and EBCs (yellow).
(J) Violin plots showing the distributions of mean vector length (MVL) for HD tuning (blue) and EB tuning (yellow).
See also Figure S1 and Table S1.

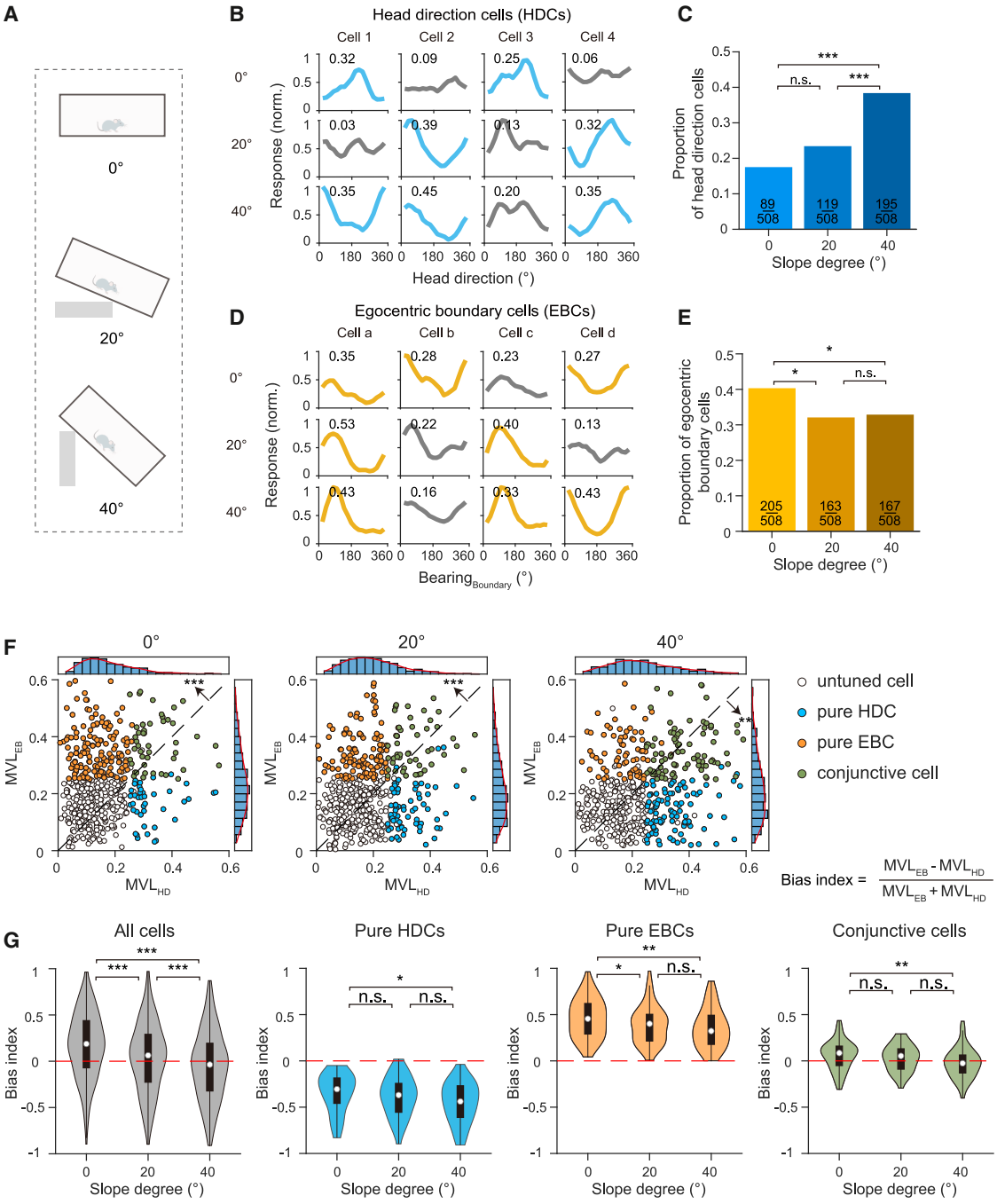

Figure 2. Enhancement of HD tuning with increased tilt angle in the sloping terrain task

(A) Diagram of the sloping terrain task.

(B) HD tuning curves of four example cells (columns) under different tilt conditions (rows): 0°, 20°, and 40°. Tuning curves are normalized. Blue, cells meeting HDC criteria; gray, cells not meeting HDC criteria; number on top, MVL value.

(C) Proportions of HDCs across different tilt conditions.

(D and E) Same as (B) and (C), but for EBCs.

(F) Scatterplots of MVL values between HD tuning and EB tuning across three tilt conditions for neurons tracked in three sessions. Each point corresponds to a neuron. White circle, untuned cell; blue circle, pure HDC; orange circle, pure EBC; green circle, conjunctive cell.

(G) Distributions of the allocentric vs. egocentric bias indices of all neurons for different tilt conditions. Left: all cells. Middle left: pure HDCs. Middle right: pure EBCs. Right: conjunctive cells.

See also Figure S2 and Table S1.

conjunctive cells under various tilt conditions. Independence statistical analyses revealed that HDCs and EBCs do not constitute distinct cell populations across different tilt angles (Figure S2J). Notably, we observed a tilt angle-dependent increase in the proportion of conjunctive cells, with higher angles corresponding to greater proportions of these cells (Figure S2K). These results indicate that as gravitational cues became more pronounced, the allocentric system was strengthened, whereas the egocentric system was weakened. In a previous study, Alexander et al. found that PPC neurons could change mean firing rate across different behavioral tasks[15] and demonstrated that PPC neurons could gain additional tuning for behaviorally relevant variables. However, we did not find significant differences in calcium event rate between pure HD/EB cells and conjunctive cells (Figures S2L and S2M). Further studies with electrophysiology techniques are required to investigate whether, with more conjunctive tuning, neurons also increase their firing rate.

Increased slope did not affect the egocentric tuning strength in the VR task

A previous study pointed out that largely independent populations of egocentric cells are recruited to represent different items across contexts.[38] Therefore, to explore whether gravitational inputs affect egocentric representation in a different behavioral task, we also recorded the activity of PPC neurons when the animals were performing a head-fixed VR task. Similar to the sloping terrain task, the VR setup included two tilt angles, 0° and 40° (Figure 3A). Two VR environments were presented: a standard world containing four landmarks (standard experiment; Figure 3B) and a modified version with adjusted landmark positions (direction-reversal experiment; Figure S3A). We identified egocentric landmark cells (ELCs) or allocentric landmark cells (ALCs) with tuning curve templates and corresponding landmark scores (STAR Methods). We also applied a visualization method (egocentric landmark rate map [ELR]; Figures 3C and 3D; STAR Methods) similar to that of the EBR. ELC would demonstrate more left-right asymmetry than that of the ALC and conjunctive cells. We quantified the extent of this egocentric coding preference with the egocentric index (EI) for each type of landmark cell (Figure 3E; STAR Methods). The results from the direction-reversal experiment confirmed that the landmark selective cells were mainly egocentric (Figure S3). For ELCs, they preferentially encoded landmarks that were spatially proximal to the animal (Figure 3F).

For four mice, the proportion of ELCs was similar between the 0° and 40° conditions (Figures 3G and 3H; 0° condition: 80/267; 40° condition: 71/228; $\chi^2 = 0.080$, $p = 0.77$). The landmark scores of ELCs showed no significant differences between the 0° and 40° conditions (Figure 3I; Wilcoxon rank-sum test, $p = 0.66$). These findings indicate that the sloping terrain in the VR task did not significantly affect the recruitment or landmark coding strength of ELCs. These results suggest that egocentric landmark coding in the VR task was only minimally influenced by gravitational cues, in contrast to egocentric boundary coding, which was weakened as gravitational signals increased. Furthermore, our data also hinted that ALCs and conjunctive landmark cells sustained stable encoding patterns under varying slope conditions (Figures 3J–3L).

Weaker consistency of HD tuning between horizontal and tilt conditions

We next explored the relationship between the preferred firing direction (PFD) of the HDCs across different tilt conditions. First, between 0° vs. 20°, clustering at 0° was less pronounced compared with the day-to-day shifts under horizontal conditions (Figures 4A–4D; 0° vs. 0° tilt: circular mean = 2°, Rayleigh test, $Z = 36.18$, $p = 3.37 \times 10^{-18}$; 0° vs. 20° tilt: circular mean = −15°, Rayleigh test, $Z = 19.14$, $p = 2.05 \times 10^{-9}$). Next, at 20° vs. 40°, PFD shifts also centered around 0°, with significantly tighter clustering at 0° than the 0° vs. 20° tilt condition (Figures 4C–4F; 20° vs. 40° tilt: circular mean = 0°, Rayleigh test, $Z = 79.32$, $p = 4.81 \times 10^{-41}$). For HDCs, HD tuning consistency significantly decreased from the horizontal to 20° tilt conditions (Figure 4M; group[0° vs. 0°] vs. group[0° vs. 20°]: Wilcoxon rank-sum test, $p = 0.013$) but did not change when the tilt increased from 20° to 40° (Figure 4M; group[0° vs. 0°] vs. group [20° vs. 40°]: $p = 0.076$). Apparently, the consistency was significantly stronger when gravitational cues were strengthened than when newly introduced (group[0° vs. 20°] vs. group[20° vs. 40°]: $p = 8.19 \times 10^{-6}$). These results indicate that, although the introduction of gravitational inputs increased the strength of HD tuning, the tuning consistency was impaired, especially between the horizontal and 20° tilt conditions. Note that the tuning strength refers to tuning curve sharpness within a single session, whereas tuning consistency measures the extent of similarity of tuning directions across sessions.

Furthermore, we confirmed that EBCs are unaffected by gravitational cues in the PFD consistency level (Figures 4G–4L and 4N). Both the introduction (0° vs. 20°: circular mean = 5°, Rayleigh test, $Z = 132.48$, $p = 1.14 \times 10^{-68}$; group[0° vs. 0°] vs. group[0° vs. 20°]: $p = 0.22$) and enhancement (20° vs. 40° tilt: circular mean = −4°, Rayleigh test, $Z = 112.30$, $p = 2.15 \times 10^{-58}$; group[0° vs. 0°] vs. group[20° vs. 40°]: $p = 0.53$; group[0° vs. 20°] vs. group[20° vs. 40°]: $p = 0.54$) of gravitational cues resulted in EBCs maintaining encoding consistency comparable to that under horizontal conditions (0° vs. 0° tilt: circular mean = −2°, Rayleigh test, Z = 110.67, $p = 3.37 \times 10^{-58}$).

In summary, EBCs exhibited significantly stronger consistency than HDCs when gravitational cues were introduced (from 0° to 20°), while HDCs achieved comparable stability to EBCs when gravitational cues were enhanced (from 20° to 40°) (Figure 4O; Wilcoxon rank-sum test: 0° vs. 0° tilt, $p = 0.003$; 0° vs. 20° tilt, $p = 4.20 \times 10^{-7}$; 20° vs. 40° tilt, $p = 0.41$). These findings were further supported by angular shifts of PFDs analysis (Figure S4). Together, we showed that gravitational inputs could interfere with the consistency of HD tuning but not EB tuning for PPC neurons.

Competition between gravitational inputs and visual inputs for HD anchoring under tilt conditions

To further disentangle the role of gravitational and visual inputs on the HDCs, we designed a cue conflict experiment in which the gravitational and visual cues were decoupled. For a specific tilt angle, there were two configurations: westward tilt and eastward tilt (Figure 5A). Thus, visual cues controlled the north-south axis of the behavioral arena, whereas the gravitational input controlled the east-west axis.

We compared its HD tuning curves under the westward tilt and the eastward tilt conditions. For some cells, the PFDs

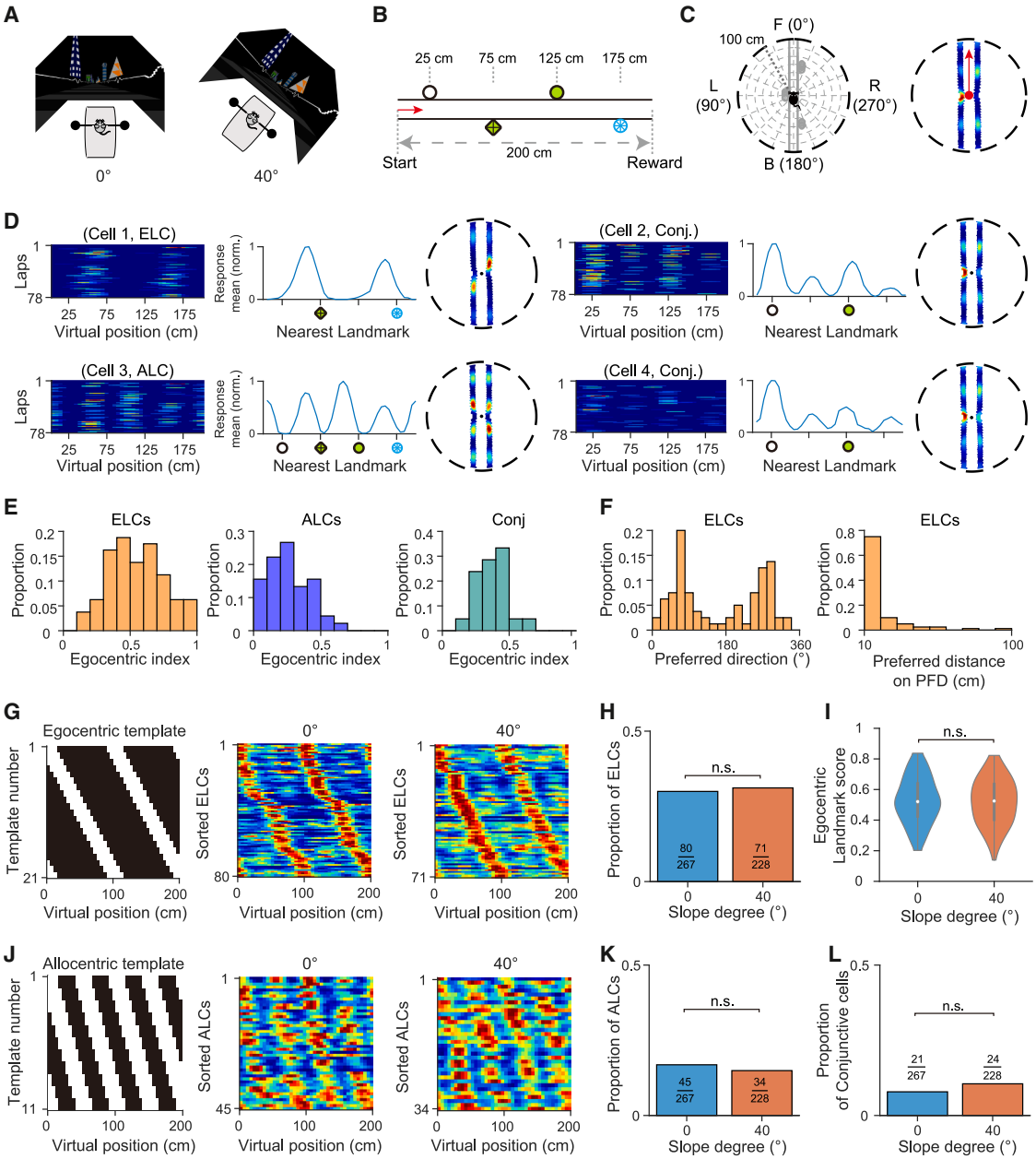

Figure 3. The increased slope had no effect on the egocentric landmark tuning in the tilted VR task

(A) Schematic diagram of the tilted virtual reality (VR) task. Left: horizontal condition. Right: 40° tilt condition.

(B) The schematic of the virtual environment for the task: standard world.

(C) Schematic for construction of the egocentric landmark rate map (ELR), which is similar to the egocentric boundary rate map (EBR) in Figure 1G. Left: egocentric landmark locations in polar coordinates at the time of calcium events for an example neuron. Landmarks within 100 cm are referenced to the current HD of the animal. Right: ELR for this neuron.

(D) Firing properties for several example landmark cells. For each cell: (left) lap-wise spatial rate maps with different firing fields. Middle: the mean spatial firing rate. Right: the ELR. Note that the ELR of an ELC demonstrates greater asymmetry compared with that of an allocentric landmark cell (ALC) or a conjunctive cell.

(E) The EI distribution of different landmark cells. Left: egocentric landmark cells (ELCs). Middle: ALCs. Right: conjunctive landmark cells (Conj).

(F) Left: the distribution of preferred firing direction (PFD) of ELCs. Right: the distribution of preferred distance on PFD (right).

(G) Left: the series of templates for detecting landmark cells with two fields (i.e., ELCs). Middle: sorted tuning curves of ELCs based on the location of their peak responses under the horizontal condition. Right: sorted tuning curves of ELCs based on the location of their peak responses under the 40° tilt condition.

(H) The proportion of ELCs under each tilt condition.

(I) The distribution of egocentric landmark scores for the population in each tilt condition.

(J and K) Same as (G) and (H), but for ALCs.

(L) The proportion of conjunctive landmark cells under each tilt condition.

See also Figure S3 and Table S1.

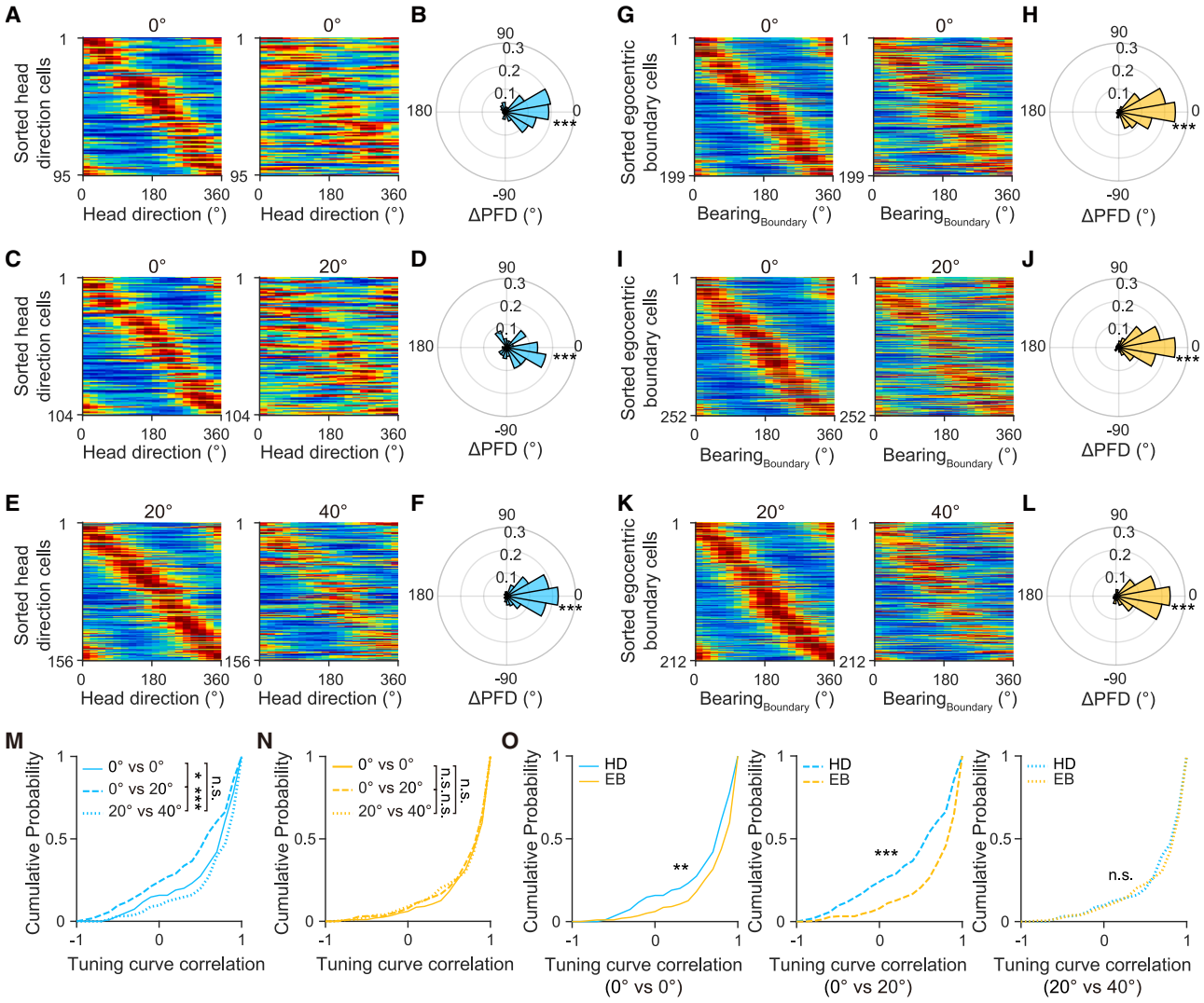

Figure 4. Weaker consistency of HD tuning between horizontal and tilt conditions

(A) HD tuning curves of HDCs across days for the horizontal condition. Cells were sorted by their PFDs on the first day of the horizontal condition.

(B) Polar histogram showing the distribution of changes in PFDs for HDCs recorded across 2 days in the horizontal condition.

(C and D) Same as (A) and (B), but for comparison between 0° and 20° tilt conditions.

(E and F) Same as (A) and (B), but for comparison between 20° and 40° tilt conditions.

(G–L) Same as (A)–(F), but for EBCs.

(M) Cumulative probability distributions of correlation coefficients between tuning curves across different tilt conditions for HDCs. Solid line, 0° vs. 0°; dashed line, 0° vs. 20°; dotted line, 20° vs. 40°.

(N) Same as (M), but for EBCs.

(O) Comparison of cumulative probability distributions between HD and EB tuning correlation. Left, 0° vs. 0°; middle, 0° vs. 20°; right, 20° vs. 40°.

See also Figure S4 and Table S1.

were similar between the two tilt conditions, indicating they were anchored to vision (Figure 5B). By contrast, for some cells, the PFDs were opposite, indicating they were anchored to gravity (Figure 5C). Thus, we categorized the HDCs into G-cells and V-cells, respectively, based on their frames of reference. G-cells are defined as those with a PFD difference between eastward and westward tilt conditions of 135°–180°, while V-cells are those with a difference of less than 45° (Figure 5D; STAR Methods). Note that although this particular working classification criterion seemed arbitrary, the bimodal distribution for the change of PFD across eastward and westward tilt conditions (Figures 5E–5G) suggested the applicability of a wide range of classification thresholds. We tracked 671 cells in both 20°W and 20°E sessions, with 258 cells identified as HDCs in 20°W or 20°E. To visualize the G-cells and V-cells at the population level, we sorted these HDC cells by their PFDs in 20°W and investigated their PFDs in 20°E (Figures 5H–5J). Results showed that the PFDs of the HDC population exhibited large angular shifts between the eastward and westward tilt (Figure 5I; 20°W vs. 20°E tilt: circular

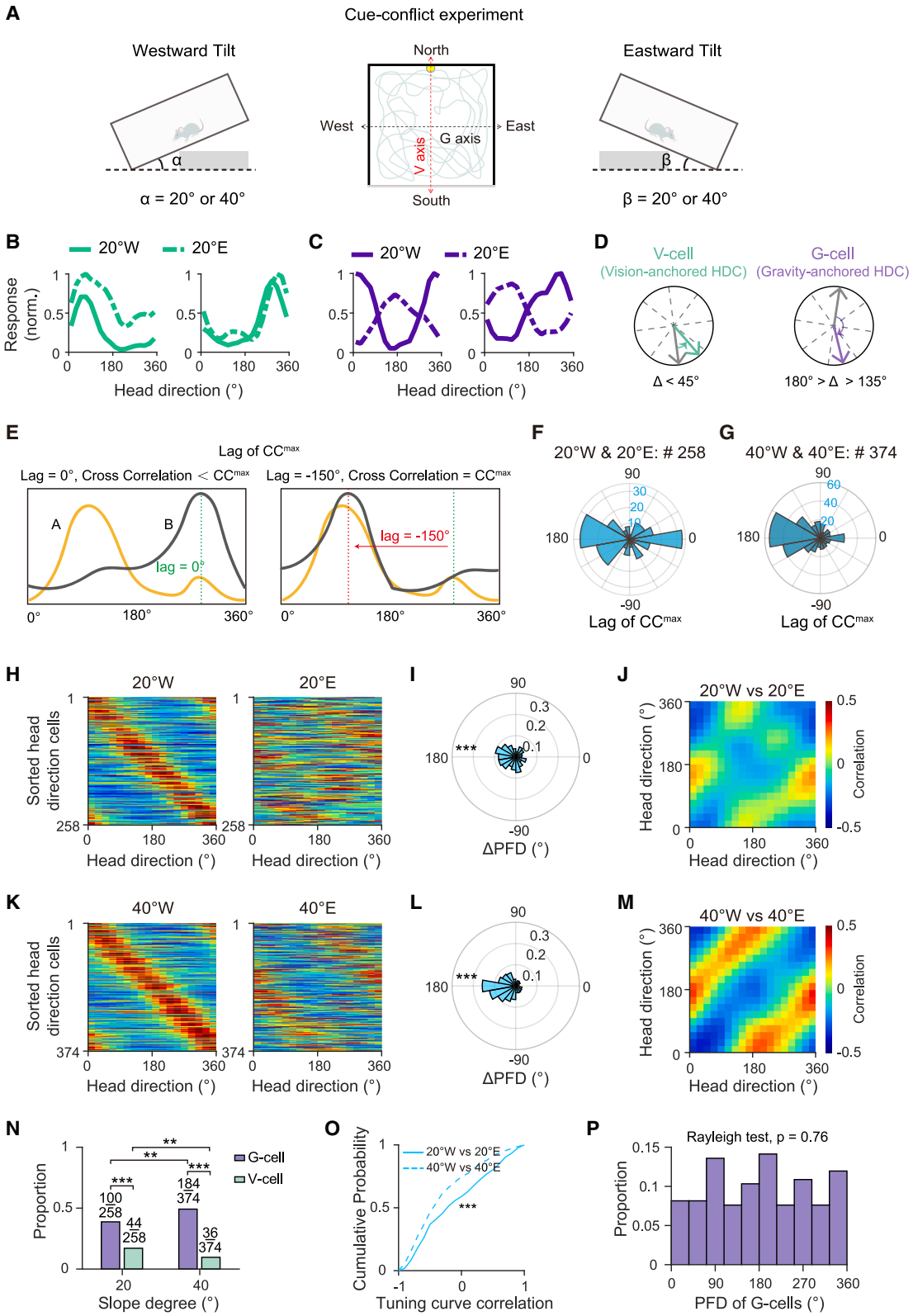

Figure 5. Competition between gravitational and visual cues for HD anchoring under opposite tilt conditions

(A) Schematic of the cue-conflict paradigm. α and β denote the westward and eastward tilt angles, respectively.

(B) Tuning curves of two example visual-cue-anchored HDCs recorded under 20°W (solid lines) and 20°E (dashed lines) tilt conditions, showing the same PFD across westward and eastward tilt conditions.

(legend continued on next page)

mean = −166°, Rayleigh test, $Z = 11.83$, $p = 6.49 \times 10^{-6}$). The effect became even more evident under the 40° tilt condition (Figures 5K–5M; 40°W vs. 40°E tilt: circular mean = −167°, Rayleigh test $Z = 74.71$, $p = 6.28 \times 10^{-35}$). For 258 HDCs in 20° tilt conditions, 38.8% (100/258) showed opposite PFD between 20°E and 20°W (G-cells), whereas 17.1% (44/258) showed similar PFD (V-cells), and there were significantly more G-cells than V-cells (Figures 5H and 5N; 20° tilt: $\chi^2 = 30.21$, $p = 3.88 \times 10^{-8}$; Figure S5H). Similarly, for 374 HDCs in 40° tilt conditions, 49.2% (184/374) showed opposite PFD between 40°E and 40°W (G-cells), whereas 9.6% (36/374) showed similar PFD (V-cells), significantly more G-cells than V-cells (Figures 5K and 5N; 40° tilt: $\chi^2 = 141.05$, $p < 0.0001$; Figure S5H). Moreover, as gravitational cues strengthened from 20° to 40° tilt, the proportion of G-cells increased while that of V-cells decreased, demonstrating a strong competitive effect of the gravitational input (Figure 5N; G-cells: $\chi^2 = 6.72$, $p = 0.0095$; V-cells: $\chi^2 = 7.62$, $p = 0.0058$). The correlation between the two 40° tilt conditions was significantly smaller than that between the two 20° tilt conditions (Figure 5O; Kolmogorov-Smirnov test, $p = 0.00027$). By contrast, EBCs maintained strong consistency throughout the cue conflict experiment, unaffected by changes in environmental cues (Figures S5A–S5G). We also observed that the PFDs of G-cells spanned all directions without being restricted to specific orientations (Figure 5P; Rayleigh test: $Z = 0.28$, $p = 0.76$). These results indicate that under conditions involving gravitational cues, HDCs could anchor to the gravitational reference frame, with the influence of visual input competing with the gravitational cue. As the tilt angle increased, the PPC neurons became biased toward the gravitational reference frame.

Switch of reference frame in some HDCs under visual and gravitational input mismatch conditions

We have demonstrated that G-cells were the dominant HDCs when gravitational input was stronger (Figure 5N). Do G-cells belong to a distinct population from V-cells, or are they transitioned from V-cells? Thus, we compared reference frames and the PFD of HDCs across sessions for the same individual HDCs in horizontal, westward, and eastward tilt conditions. We classified all the HDCs detected in the horizontal condition as V-cells, as when the navigational plane is flat, gravitational information does not constitute a polarizing cue (STAR Methods).

From the horizontal to 20° tilt conditions, 671 cells were tracked across three sessions (horizontal, 20°E, and 20°W), and 140 cells were identified as HDCs in the horizontal session (Figure S6A). Under the 20° tilt conditions, approximately 22% (31/140) of these HDCs switched to gravitational cue anchoring (V to G), while over 28% (40/140) remained anchored to visual cues (V to V) (Figures 6A and 6B; $\chi^2 = 1.53$, $p = 0.22$). From the horizontal to 40° tilt conditions, 721 cells were tracked across three sessions (horizontal, 40°E, and 40°W), and 143 cells were identified as HDCs in the horizontal session (Figure S6A). Under the 40° tilt conditions, 33.5% (48/143) of HDCs adopted gravitational cue anchoring, while the proportion of HDCs maintaining visual cue anchoring dropped to around 20% (29/143, Figures 6C and 6D; $\chi^2 = 6.42$, $p = 0.011$). Additionally, we examine the cells that were identified as HDCs in all three sessions (43 cells for 20° tilt, 37 cells for 40° tilt; Figure S6A). From horizontal to 20° tilt conditions, approximately 5% (2/43) of HDCs switched to gravitational cue anchoring (V to G), while over 50% (22/43) remained anchored to visual cues (V to V). From horizontal to 40° tilt conditions, 48.6% (18/37) of HDCs switched to gravitational cue anchoring (V to G), while only 11% (4/37) remained anchored to visual cues (V to V) (Figure S6B). In addition, the G-cells could also be derived from the non-HDC cells in horizontal condition (Figure S6C).

We also examined the reference frame selection of HDCs between 20° and 40° tilt conditions (Figure 6E). A total of 412 cells were tracked across 4 sessions (20°E, 20°W, 40°E, and 40°W), out of which 67 cells were identified as G-cells and 20 cells were identified as V-cells under 20° tilt conditions. G-cells identified under the 20° tilt conditions largely maintained their anchoring to gravitational cues when the tilt was increased to 40° (Figure 6F; G to G vs. G to V: $\chi^2 = 44.94$, $p = 2.03 \times 10^{-11}$). By contrast, some V-cells switched to the gravitational reference frame (Figure 6F; V to G vs. V to V: $\chi^2 = 0.11$, $p = 0.74$).

We summarized the recruitment dynamics and reference frame selection of HDCs under the influence of gravitational cues (Figure 6G). Under the horizontal condition, a small proportion of PPC neurons were recruited as HDCs, and the visual reference frame functions dominated. When gravitational cues were introduced, the gravitational reference frame significantly influenced HD tuning. On the one hand, previously non-HDC neurons turned into HDC, with most of them anchored to gravitational cues (Figure S6C). Additionally, some existing V-cells switched to the gravitational reference frame, while others

(C) Tuning curves of two example gravitational-cue-anchored HDCs under 20°W (solid lines) and 20°E (dashed lines) tilt conditions, each exhibiting a 180° PFD reversal between westward and eastward tilt conditions.
(D) Definitions of gravity-anchored HDC (G-cell) and vision-anchored HDC (V-cell).
(E) Schematic of the analysis of the lag of CC^{max}.
(F) The bimodal distribution of lags of CC^{max} for HDCs under 20° tilt conditions.
(G) Same as (F), but for 40° tilt conditions.
(H) Tuning curves of HDCs for 20°W vs. 20°E tilt conditions. Cells were sorted by their PFDs under 20°W.
(I) Distribution of PFD shifts for HDCs between 20°W and 20°E tilt conditions.
(J) Population vector correlation for HDCs between 20°W and 20°E tilt conditions.
(K–M) Same as (H)–(J), but for HDCs between 40°W and 40°E tilt conditions.
(N) Proportions of G-cells and V-cells under 20° and 40° tilt conditions.
(O) Cumulative probability distributions of Pearson correlation coefficients for tuning curves of HDCs across the two configurations of the 20° tilt condition (solid line) and the 40° tilt condition (dashed line).
(P) Distribution of PFDs for G-cells under 40° tilt conditions.
See also Figure S5 and Table S1.

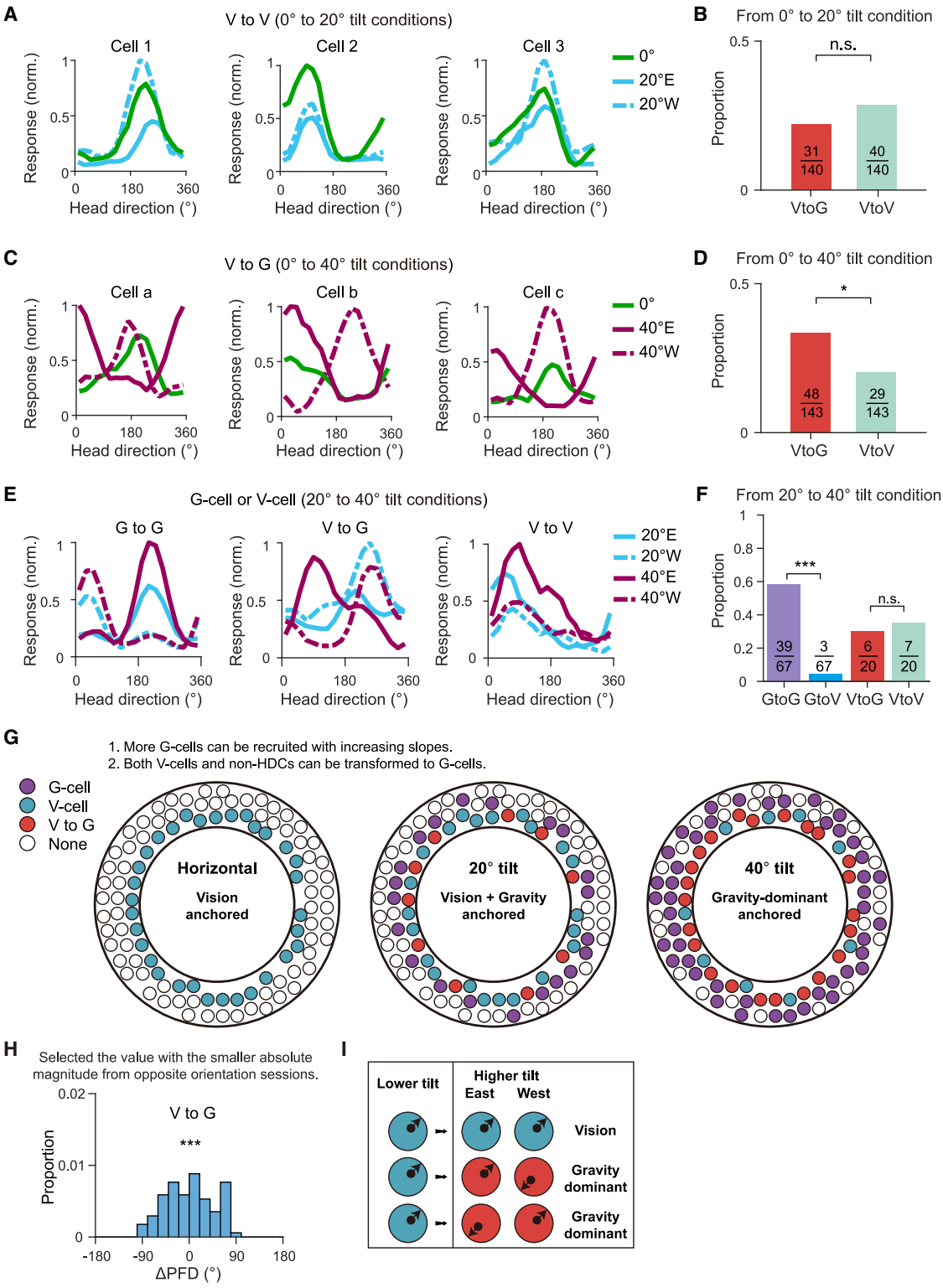

Figure 6. Reference frame switches in some HDCs under mismatched visual and gravitational cues

(A) HD tuning curves for three example HDCs from 0° (green line) to 20° (blue lines) tilt conditions. The solid blue line and dashed blue line denote the tuning curves under the 20°E and 20°W tilt configurations, respectively.

(B) Histograms showing the proportions of HDCs (identified at 0°) that switched to G-cells or V-cells under 20° tilt conditions (20°W and 20°E).

(C) Same as (A), but for 0°–40° tilt conditions. All three cells were from a single animal and were categorized as G-cells under the 40° tilt conditions, with their peaks offset by ~180° (two purple lines). Note that one of the purple curves aligns with the green curve.

(legend continued on next page)

maintained the visual cues anchoring. As gravitational cues were further strengthened, HD became stronger, and the gravitational reference frame became dominant.

Furthermore, when an HDC switched from the visual to the gravitational reference frame (V to G), one of the PFDs in the two configurations (eastward and westward tilts) remained similar to the PFD when they were anchored to the visual reference frame (Figures 6C and 6E). Different G-cells may choose to align the PFD in the eastward or westward configurations to the visual PFD (Figures S6D–S6O), even for the cells in the same animal (Figure 6C). We quantified the change of PFD after the switch of reference frames and found that the one with the smaller magnitude clustered around zero (Figure 6H, $n = 85$ cells; circular mean = $-1.86°$, Rayleigh test, $Z = 42.94$, $p = 1.94 \times 10^{-22}$), confirming the observations that the choice of HD was not random, and G-cells inherited a preferred direction from when they were anchoring to the visual reference frame (Figure 6I). In addition, this may also imply that visual input may also have some influence over G-cells under some conditions. This was supported by the fact that HD preferences of PPC cells remained similar in the dark on the tilted surface (Figure S7). In summary, our results indicate that as gravitational cues intensified, non-HDC cells could be recruited to serve as gravity-anchored cells, and V-cells could switch to the gravitational reference frame.

DISCUSSION

By manipulating the tilt degree of the behavioral arena, we found a decoupling between allocentric HD and egocentric boundary representation: allocentric HD representation became stronger, whereas egocentric boundary representation was attenuated, yet egocentric landmark coding remained intact. At the population level, the preferred direction of HDCs changed when the arena was tilted, largely due to the emergence of a subtype of HDCs anchored to the gravitational frame of reference. The proportion of G-cells increased as vision-anchored V-cells and non-HDCs converted into G-cells. The preferred HDs of G-cells were related to the direction when they were visually anchored in horizontal condition.

Differential control of egocentric and allocentric representation by gravity

Gravitational fields are present for all animals on Earth. Thus, both perception and sensorimotor control rely on the appropriate integration of gravity information.[39] For example, gravity can distort the perception of 3D object shape based on visual and somatosensory inputs.[40] Many animals have gravity-sensing otoliths. This vestibular information from the otoliths provides cues for navigation in different body tilts. Also, proprioception from the muscles and joints varies across sloping terrains, offering an additional polarization cue for navigation. Thus, the term "gravity" in this study indicates the spectrum of signals related to gravity. The otolith signal was also critical for the function of HDCs.[41] We found that with increasing slopes of the navigating plane, the allocentric HDC anchored to gravity began to prevail, although the PPC has been hypothesized to be dominated by egocentric representation. The increase of HD tuning on a tilted navigation plane was not specific to any specific cell class (Figures 2F and 2G). This suggests that the PPC, as an association cortex, could readily incorporate tuning for additional behavioral variables, rather than a dedicated circuit for a specific function. The parietal cortex can employ diverse reference frames representing visual[1,7] and vestibular information.[4] Chen et al.[42] found that, depending on the specific strategy of gaze, vestibular heading information could be switched from an egocentric to an allocentric frame of reference. In our results, with a simple navigation task on an inclined surface, we found a gradual increase in allocentric HD signal anchored to gravity and a relatively weaker decrease in egocentric representation. The dominance of the gravitational over the visual reference frame reported here is consistent with and reinforces the idea that gravity plays a central role in spatial perception.[43–45]

What are the possible mechanisms for the gravity-dependent HD tuning? When mice are allowed to rotate continuously on an orientable platform, HDCs in the thalamus, RSC, and cingulum bundle are shown to conjunctively represent azimuth and tilt.[35] As the PPC has bidirectional connectivity with the thalamus and RSC, gravitational input may reach the PPC via these systems. A primate study has shown that the visual object representations in parietal neurons are sensitive to the gravity axis.[43] Laurens et al. demonstrated that primate anterodorsal thalamic nucleus (ADN) cells can represent tilt information.[31] In addition, brain state could modulate the HD system in the thalamus,[46] thus dynamically adjusting the gain of the gravity-centered HD signal when there is sensory conflict, consistent with the finding that directional tuning could be behavior dependent.[47,48] The hippocampus could be influenced by gravitational inputs,[24–26,29,32,33] and there is bidirectional communication between PPC and the hippocampus.[49] Thus, it is also possible that PPC provides gravitational information to the hippocampus.

Egocentric representation of external items has been the focus of extensive research.[8,13,37,38,50–62] The differential control of egocentric and gravity-centered allocentric representation suggests that the circuitry in PPC permits a task-specific dynamic modulation of population tuning of behavioral

(D) Same as (B), but for 40° tilt conditions (40°W and 40°E).
(E) Tuning curves, for example, HDCs from 20° to 40° tilts. G to G, V to G, and V to V represent the switch of frame preference from 20° to 40° tilt conditions.
(F) Proportions of HDCs recorded under 20° tilt conditions that switched or maintained their frame preferences under 40° tilt conditions.
(G) Diagrams showing the recruitment of different categories of HDCs with increasing slopes.
(H) Distribution of PFD changes for cells that switched from visual to gravitational reference frame (V to G). For each cell, we took the smaller absolute angular difference between its PFD under the visual-anchoring condition and each of its two PFDs under the higher-tilt gravity-anchoring condition. The histogram shows that, after the reference frame switches from visual to gravity, one of each cell's gravity-anchored PFDs realigns closely with its original visual-anchored PFD.
(I) Diagram illustrating how the PFDs are determined from lower-tilt to higher-tilt conditions (e.g., 0° to 20° tilt, 0° to 40° tilt, or 20° to 40° tilt). Blue: HDCs with visual reference frame. Red: HDCs with gravitational reference frame. Arrow indicates the PFD of the respective condition.
See also Figures S6 and S7 and Table S1.

variables.[16,42] The egocentric boundary representation was less affected, which suggests that the egocentric representation might be more concerned with the local sensory feature than the gravity information. By contrast, the allocentric system may more readily incorporate global and contextual information, including gravitational cues. As gravitational cues intensified, the egocentric representation of landmarks in the head-fixed VR task remained unchanged. This may reflect the task-dependence of egocentric processing or the recruitment of distinct egocentric cell populations—with different sensitivities to gravity—in each paradigm. Given that the PPC is at one end of the egocentric-allocentric transformation circuit and the extensive interconnectivity between the PPC and the RSC, similar results might be likely to occur in the RSC (Figure S2D).[2,5,6]

The egocentric representation system is likely to be heterogeneous, comprised of diverse functional cell types. ELCs represent discrete visual landmarks in the VR environment, whereas EBCs convey egocentric spatial information about continuous environmental boundaries. These two systems possibly reflect the different topological properties of the environment. Environmental boundaries are continuous objects, whereas visual landmarks are discrete. They likely invoke different visual optic flow patterns. It is possible that the egocentric representation of the continuous boundaries needs to integrate more global contextual input (e.g., gravitational information) than that of local landmarks.

The functional difference between ELC and EBC is reminiscent of EBC subtypes. For example, LaChance and Hasselmo have shown that the EBCs in the POR react differently to environmental symmetries from the EBCs in the RSC.[63] In addition, these functional differences of EBC could be explained and modeled by the properties of different visual projection pathways (i.e., superior colliculus to POR and V1 to RSC).[64] In addition, related to the edges of the environment, egocentric representation of arena vertices has also been reported.[65]

There is an intriguing functional parallel between the open-field and head-fixed VR conditions. In both tasks, there are egocentric representations, conjunctive representations (Figure 3; STAR Methods), and allocentric representations. These categories of cell types may reflect a shared wiring principle for the coordinate transformation across different functional systems in the navigation circuit. Conjunctive cells that are sensitive to both egocentric and allocentric reference frames may provide the network basis for converting the two coordinate systems, as proposed in various models.[2,5,6,13,21,51] A similar computation has also been suggested to explain eye-head-trunk coordinate transformation in primates.[66,67] Future studies that combine circuit mapping with functional studies are needed to test quantitatively the models of coordinate transformation. It would be important to investigate the egocentric landmark processing in real-world one-dimensional tasks in the future.

Two types of HDCs

HDCs have been discovered across many regions of the limbic system.[68,69] Recent work suggests that HDCs may consist of different subnetworks.[70–76] For example, they may be driven by different sensory modalities, e.g., vestibular and visual input,[71] although usually visual reference predominates.[77] Here, we find that HDCs in PPC could be divided into a gravity-anchored population and a visual cue-anchored population. Interestingly, the influence of gravity was not limited to the cardinal directions related to the manipulation but also other angles (Figure 5P), suggesting that the HD network is tightly coupled.[68,69]

Thus, our results suggest that, in addition to being critical for maintaining HD tuning,[41,78,79] the gravitational signal served as the preferred reference frame for anchoring HD representation when there was a conflict between visual and gravitational reference frames. As the same HDCs could switch reference frames with increasing slopes of the behavioral plane in our results, the G-cells and V-cells are not mutually exclusive populations of neurons. This provides a suitable system for studying the dynamic switching of reference frames. In addition, after switching to the gravity-centered reference frame, the preferred HD was aligned with the preferred direction (or the opposite direction) when the cells were visually anchored. This suggests that the reference frame re-anchoring is different from global remapping. This strategy may incur less perceptual change between conditions. Note that the change of reference frames for a proportion of HDCs could be described by partial remapping. This partial remapping of HDCs is similar to the heterogeneous behavior of HDCs as reported in earlier findings[71,72] when cues are put into conflict. We speculate that the appearance of G-cells may reflect the heterogeneous responses of PPC neurons. In most previous studies of HDC during 3D navigation in rodents,[34,80,81] the HDCs were recorded from the anterior dorsal nucleus of the thalamus (ADN). The ADN cells have been shown to be coherent[77,82] and have been hypothesized to be a single HD attractor. However, the HDCs in other brain regions are less homogeneous. For instance, where there are conflicting visual cue arrangements in two connected compartments, there are bidirectional HDC in area 30 of the RSC, but not area 29 of the RSC.[71] The finding that there are subcategories of HDC in PPC further supports that the HD system integrates diverse inputs from vision and gravity, and there may exist multiple HD attractors within a single brain region. Our results are also compatible with the scenario that PPC is influenced by a single attractor, and there are multiple feedback signals (vision- or gravity-based) to the attractor or to the PPC itself. The exact implementation would require further functional dissection of the upstream circuit.

There are multiple brain areas involved in the representation of the HD of the animal.[68] HDCs in the PPC are tightly integrated with egocentric information, which may reflect the coordination transformation hypothesized to happen in the retrosplenial-parietal network.[2,5,6,13,21] These all suggest that the HD system in PPC could not be a pure HD attractor. Similar non-attractor HD representation (landmark-controlled bidirectional firing) has been reported in the RSC.[71] However, the distinct behaviors of the gravity- and vision-controlled population of HD hint at their control by multiple upstream attractors.

Spatial representation in 3D environments has gone through extensive studies.[24–36] Many of them are concerned with the spatial and directional representation when animals' locomotion is not confined to a single degree of freedom in a session, i.e., where there is full 3D representation. Both place cells and grid cells are affected on the inclined locomotion plane in the form of remapping or degraded quality.[25,27,32] Studies with the

inclined plane have found that HDCs are only sensitive to azimuth.[83,84] Here, we find that with the minimization of distal visual cues outside of the behavioral arena, the conflict between gravity and local visual cues induced anchoring to the gravitational reference frame for some HDCs. This is in line with a previous study, which found that the slope of the terrain could serve as an orienting cue for hippocampal place cells when visual orienting information is absent.[85] Thus, the G-cells may provide the necessary input for the hippocampus to create an oriented spatial map to improve orientation.[86,87]

Behavioral tasks play essential roles in determining the reference frames during navigation. Depending on the behavioral demand in the current context, the animals may adopt different behavioral strategies and thus frames of reference to organize spatial information. For example, Taube et al.[80] demonstrated that depending on how the animals were introduced into the vertical navigational plane, the HDC firing could be anchored either to the local reference frame of the vertical platform or to the room-based coordinate. In a different study,[34] when animals were restrained and rotated passively in various 3D planes, the tuning of HDC was not affected by pitch or roll up to 90° from the horizontal plane. Our task design differed from these previous studies in several aspects. There are only two sets of tilt directions: eastward and westward tilt. It is possible that the navigational system creates two discrete contexts, with the gravitational information being the most discriminative of the two contexts. Besides, within a single session, the gravitational configuration remains fixed, in contrast to the more dynamic rotation in Shinder and Taube's experiment. Furthermore, the gravitational cue is robust and serves as an important prior.[45] Taken together, these might explain the switch from a visual reference frame to a gravitational reference frame for some HDCs in our study.

We also found that egocentric cells were more conjunctive with allocentric HD as the plane tilt increased. This is consistent with a previous study showing that the HDCs can dynamically change the degree of conjunctive tuning.[47] The mixed selectivity may facilitate more efficient processing of both gravity-centered allocentric HD input and egocentric information on an inclined surface.[75,88–92]

In all, both the dynamic recruitment of PPC cells employing different reference systems with varying gravitational inputs and the re-anchoring of cells to types of external references revealed a flexible coding rule for spatial information during natural behavior.

RESOURCE AVAILABILITY

Lead contact

Further information and requests for resources should be directed to and will be fulfilled by the lead contact, Xiaojing Chen (chenxj@sustech.edu.cn).

Materials availability

This study did not generate new unique reagents.

Data and code availability

- Data reported in this study are available at GitHub under the accession code: https://github.com/XiaojingChenLab/GravityPPC. The link is also listed in the key resources table. Due to the large file size, the original calcium imaging videos are available upon request.
- This study does not report original codes.
- Any additional information required to reanalyze the data reported in this paper is available from the lead contact upon request.

ACKNOWLEDGMENTS

We thank Chun Xu and Chenglin Miao for discussions. This work was supported by the following grants: STI2030-Major projects 2022ZD0205000 (C.W.), STI2030-Major projects 2022ZD0205500 (X.C.), The Strategic Priority Research Program of the Chinese Academy of Sciences XDB1010102 (C.W.), the National Natural Science Foundation of China 32471084 (C.W.), the National Natural Science Foundation of China 32471085 (X.C.), the Lingang Laboratory LG-TKN-202204-01 (C.W.), the Shenzhen Science and Technology Program JCYJ20240813100516022 (J.Z.), the National Natural Science Foundation of China 32400849 (N.C.), the Shenzhen Science and Technology Innovation Commission JCYJ20241202124921029 (C.W.), and the Guangdong Provincial Key Laboratory of Brain Connectome and Behavior 2023B1212060055 (C.W.).

AUTHOR CONTRIBUTIONS

J.Z., B.A., N.C., C.W., and X.C. designed the experiments; J.Z., B.A., and Q.D. collected the data; J.Z. and N.C. analyzed the data; J.Z., C.W., X.C., and N.C. provided supervision and funding; J.Z., C.W., and X.C. wrote the manuscript; and all authors provided comments and feedback on the manuscript.

DECLARATION OF INTERESTS

The authors declare no competing interests.

STAR★METHODS

Detailed methods are provided in the online version of this paper and include the following:

- KEY RESOURCES TABLE
- EXPERIMENTAL MODEL AND SUBJECT DETAILS
  - Animals
- METHOD DETAILS
  - Surgical Procedures
  - Histology
  - The horizontal open field foraging task
  - The sloping terrain task
  - The tilted virtual reality task
  - Data collection
- QUANTIFICATION AND STATISTICAL ANALYSIS
  - Behavioral variables and neuronal signal extraction
  - Data analysis

SUPPLEMENTAL INFORMATION

Supplemental information can be found online at https://doi.org/10.1016/j.cub.2025.08.048.

Received: April 28, 2025
Revised: July 21, 2025
Accepted: August 20, 2025
Published: September 17, 2025

REFERENCES

1. Andersen, R.A., Snyder, L.H., Bradley, D.C., and Xing, J. (1997). Multimodal representation of space in the posterior parietal cortex and its use in planning movements. Annu. Rev. Neurosci. *20*, 303–330. https://doi.org/10.1146/annurev.neuro.20.1.303.
2. Byrne, P., Becker, S., and Burgess, N. (2007). Remembering the past and imagining the future: a neural model of spatial memory and imagery. Psychol. Rev. *114*, 340–375. https://doi.org/10.1037/0033-295X.114.2.340.
3. Knierim, J.J., and Hamilton, D.A. (2011). Framing spatial cognition: neural representations of proximal and distal frames of reference and their roles

in navigation. Physiol. Rev. *91*, 1245–1279. https://doi.org/10.1152/physrev.00021.2010.

4. Chen, X., DeAngelis, G.C., and Angelaki, D.E. (2013). Diverse spatial reference frames of vestibular signals in parietal cortex. Neuron *80*, 1310–1321. https://doi.org/10.1016/j.neuron.2013.09.006.
5. Clark, B.J., Simmons, C.M., Berkowitz, L.E., and Wilber, A.A. (2018). The retrosplenial-parietal network and reference frame coordination for spatial navigation. Behav. Neurosci. *132*, 416–429. https://doi.org/10.1037/bne0000260.
6. Bicanski, A., and Burgess, N. (2020). Neuronal vector coding in spatial cognition. Nat. Rev. Neurosci. *21*, 453–470. https://doi.org/10.1038/s41583-020-0336-9.
7. Sasaki, R., Anzai, A., Angelaki, D.E., and DeAngelis, G.C. (2020). Flexible coding of object motion in multiple reference frames by parietal cortex neurons. Nat. Neurosci. *23*, 1004–1015. https://doi.org/10.1038/s41593-020-0656-0.
8. Wang, C., Chen, X., and Knierim, J.J. (2020). Egocentric and allocentric representations of space in the rodent brain. Curr. Opin. Neurobiol. *60*, 12–20. https://doi.org/10.1016/j.conb.2019.11.005.
9. Geva-Sagiv, M., Romani, S., Las, L., and Ulanovsky, N. (2016). Hippocampal global remapping for different sensory modalities in flying bats. Nat. Neurosci. *19*, 952–958. https://doi.org/10.1038/nn.4310.
10. Chen, L.L., Lin, L.H., Barnes, C.A., and McNaughton, B.L. (1994). Head-direction cells in the rat posterior cortex. II. Contributions of visual and ideothetic information to the directional firing. Exp. Brain Res. *101*, 24–34. https://doi.org/10.1007/BF00243213.
11. Harvey, C.D., Coen, P., and Tank, D.W. (2012). Choice-specific sequences in parietal cortex during a virtual-navigation decision task. Nature *484*, 62–68. https://doi.org/10.1038/nature10918.
12. Nitz, D.A. (2012). Spaces within spaces: rat parietal cortex neurons register position across three reference frames. Nat. Neurosci. *15*, 1365–1367. https://doi.org/10.1038/nn.3213.
13. Wilber, A.A., Clark, B.J., Forster, T.C., Tatsuno, M., and McNaughton, B.L. (2014). Interaction of egocentric and world-centered reference frames in the rat posterior parietal cortex. J. Neurosci. *34*, 5431–5446. https://doi.org/10.1523/JNEUROSCI.0511-14.2014.
14. Mimica, B., Dunn, B.A., Tombaz, T., Bojja, V.P.T.N.C.S., and Whitlock, J.R. (2018). Efficient cortical coding of 3D posture in freely behaving rats. Science *362*, 584–589. https://doi.org/10.1126/science.aau2013.
15. Alexander, A.S., Tung, J.C., Chapman, G.W., Conner, A.M., Shelley, L.E., Hasselmo, M.E., and Nitz, D.A. (2022). Adaptive integration of self-motion and goals in posterior parietal cortex. Cell Rep. *38*, 110504. https://doi.org/10.1016/j.celrep.2022.110504.
16. Lee, J.J., Krumin, M., Harris, K.D., and Carandini, M. (2022). Task specificity in mouse parietal cortex. Neuron *110*, 2961–2969.e5. https://doi.org/10.1016/j.neuron.2022.07.017.
17. Nitz, D.A. (2006). Tracking route progression in the posterior parietal cortex. Neuron *49*, 747–756. https://doi.org/10.1016/j.neuron.2006.01.037.
18. Rancz, E.A., Moya, J., Drawitsch, F., Brichta, A.M., Canals, S., and Margrie, T.W. (2015). Widespread vestibular activation of the rodent cortex. J. Neurosci. *35*, 5926–5934. https://doi.org/10.1523/JNEUROSCI.1869-14.2015.
19. Andersen, R.A., and Mountcastle, V.B. (1983). The influence of the angle of gaze upon the excitability of the light-sensitive neurons of the posterior parietal cortex. J. Neurosci. *3*, 532–548. https://doi.org/10.1523/JNEUROSCI.03-03-00532.1983.
20. Wilber, A.A., Skelin, I., Wu, W., and McNaughton, B.L. (2017). Laminar organization of encoding and memory reactivation in the parietal cortex. Neuron *95*, 1406–1419.e5. https://doi.org/10.1016/j.neuron.2017.08.033.
21. McNaughton, B.L., Knierim, J.J., and Wilson, M.A. (1995). Vector encoding and the vestibular foundations of spatial cognition: Neurophysiological and computational mechanisms. In The Cognitive Neurosciences (The MIT Press), pp. 585–595.
22. Alexander, A.S., Place, R., Starrett, M.J., Chrastil, E.R., and Nitz, D.A. (2023). Rethinking retrosplenial cortex: Perspectives and predictions. Neuron *111*, 150–175. https://doi.org/10.1016/j.neuron.2022.11.006.
23. Chen, L.L., Lin, L.H., Green, E.J., Barnes, C.A., and McNaughton, B.L. (1994). Head-direction cells in the rat posterior cortex. I. Anatomical distribution and behavioral modulation. Exp. Brain Res. *101*, 8–23. https://doi.org/10.1007/BF00243212.
24. Knierim, J.J., McNaughton, B.L., and Poe, G.R. (2000). Three-dimensional spatial selectivity of hippocampal neurons during space flight. Nat. Neurosci. *3*, 209–210. https://doi.org/10.1038/72910.
25. Knierim, J.J., and McNaughton, B.L. (2001). Hippocampal place-cell firing during movement in three-dimensional space. J. Neurophysiol. *85*, 105–116. https://doi.org/10.1152/jn.2001.85.1.105.
26. Hayman, R., Verriotis, M.A., Jovalekic, A., Fenton, A.A., and Jeffery, K.J. (2011). Anisotropic encoding of three-dimensional space by place cells and grid cells. Nat. Neurosci. *14*, 1182–1188. https://doi.org/10.1038/nn.2892.
27. Hayman, R.M.A., Casali, G., Wilson, J.J., and Jeffery, K.J. (2015). Grid cells on steeply sloping terrain: evidence for planar rather than volumetric encoding. Front. Psychol. *6*, 925. https://doi.org/10.3389/fpsyg.2015.00925.
28. Taube, J.S. (2011). Head direction cell firing properties and behavioural performance in 3-D space. J. Physiol. *589*, 835–841. https://doi.org/10.1113/jphysiol.2010.194266.
29. Yartsev, M.M., and Ulanovsky, N. (2013). Representation of three-dimensional space in the hippocampus of flying bats. Science *340*, 367–372. https://doi.org/10.1126/science.1235338.
30. Finkelstein, A., Derdikman, D., Rubin, A., Foerster, J.N., Las, L., and Ulanovsky, N. (2015). Three-dimensional head-direction coding in the bat brain. Nature *517*, 159–164. https://doi.org/10.1038/nature14031.
31. Laurens, J., Kim, B., Dickman, J.D., and Angelaki, D.E. (2016). Gravity orientation tuning in macaque anterior thalamus. Nat. Neurosci. *19*, 1566–1568. https://doi.org/10.1038/nn.4423.
32. Porter, B.S., Schmidt, R., and Bilkey, D.K. (2018). Hippocampal place cell encoding of sloping terrain. Hippocampus *28*, 767–782. https://doi.org/10.1002/hipo.22966.
33. Casali, G., Bush, D., and Jeffery, K. (2019). Altered neural odometry in the vertical dimension. Proc. Natl. Acad. Sci. USA *116*, 4631–4636. https://doi.org/10.1073/pnas.1811867116.
34. Shinder, M.E., and Taube, J.S. (2019). Three-dimensional tuning of head direction cells in rats. J. Neurophysiol. *121*, 4–37. https://doi.org/10.1152/jn.00880.2017.
35. Angelaki, D.E., Ng, J., Abrego, A.M., Cham, H.X., Asprodini, E.K., Dickman, J.D., and Laurens, J. (2020). A gravity-based three-dimensional compass in the mouse brain. Nat. Commun. *11*, 1855. https://doi.org/10.1038/s41467-020-15566-5.
36. Ginosar, G., Aljadeff, J., Burak, Y., Sompolinsky, H., Las, L., and Ulanovsky, N. (2021). Locally ordered representation of 3D space in the entorhinal cortex. Nature *596*, 404–409. https://doi.org/10.1038/s41586-021-03783-x.
37. Alexander, A.S., Carstensen, L.C., Hinman, J.R., Raudies, F., Chapman, G.W., and Hasselmo, M.E. (2020). Egocentric boundary vector tuning of the retrosplenial cortex. Sci. Adv. *6*, eaaz2322. https://doi.org/10.1126/sciadv.aaz2322.
38. Cheng, N., Dong, Q., Zhang, Z., Wang, L., Chen, X., and Wang, C. (2024). Egocentric processing of items in spines, dendrites, and somas in the retrosplenial cortex. Neuron *112*, 646–660.e8. https://doi.org/10.1016/j.neuron.2023.11.018.
39. White, O., Gaveau, J., Bringoux, L., and Crevecoeur, F. (2020). The gravitational imprint on sensorimotor planning and control. J. Neurophysiol. *124*, 4–19. https://doi.org/10.1152/jn.00381.2019.
40. Morfoisse, T., Herrera Altamira, G.H., Angelini, L., Clément, G., Beraneck, M., McIntyre, J., and Tagliabue, M. (2024). Modality-independent effect of gravity in shaping the internal representation of 3D space for visual and

haptic object perception. J. Neurosci. *44*, e2457202023. https://doi.org/10.1523/JNEUROSCI.2457-20.2023.

41. Yoder, R.M., and Taube, J.S. (2009). Head direction cell activity in mice: robust directional signal depends on intact otolith organs. J. Neurosci. *29*, 1061–1076. https://doi.org/10.1523/JNEUROSCI.1679-08.2009.
42. Chen, X., DeAngelis, G.C., and Angelaki, D.E. (2018). Flexible egocentric and allocentric representations of heading signals in parietal cortex. Proc. Natl. Acad. Sci. USA *115*, E3305–E3312. https://doi.org/10.1073/pnas.1715625115.
43. Rosenberg, A., and Angelaki, D.E. (2014). Gravity influences the visual representation of object tilt in parietal cortex. J. Neurosci. *34*, 14170–14180. https://doi.org/10.1523/JNEUROSCI.2030-14.2014.
44. Lacquaniti, F., Bosco, G., Gravano, S., Indovina, I., La Scaleia, B., Maffei, V., and Zago, M. (2015). Gravity in the brain as a reference for space and time perception. Multisens. Res. *28*, 397–426. https://doi.org/10.1163/22134808-00002471.
45. Jörges, B., and López-Moliner, J. (2017). Gravity as a strong prior: implications for perception and action. Front. Hum. Neurosci. *11*, 203. https://doi.org/10.3389/fnhum.2017.00203.
46. Blanco-Hernández, E., Balsamo, G., Preston-Ferrer, P., and Burgalossi, A. (2024). Sensory and behavioral modulation of thalamic head-direction cells. Nat. Neurosci. *27*, 28–33. https://doi.org/10.1038/s41593-023-01506-1.
47. Finkelstein, A., Ulanovsky, N., Tsodyks, M., and Aljadeff, J. (2018). Optimal dynamic coding by mixed-dimensionality neurons in the head-direction system of bats. Nat. Commun. *9*, 3590. https://doi.org/10.1038/s41467-018-05562-1.
48. Nau, M., Navarro Schröder, T., Frey, M., and Doeller, C.F. (2020). Behavior-dependent directional tuning in the human visual-navigation network. Nat. Commun. *11*, 3247. https://doi.org/10.1038/s41467-020-17000-2.
49. Zheng 征亦诚, Y., Zhou 周信羽, X., Moseley, S.C., Ragsdale, S.M., Alday, L.J., Wu 吴畏, W., and Wilber, A.A. (2025). A hippocampal–parietal network for reference frame coordination. J. Neurosci. *45*, e1782242025. https://doi.org/10.1523/JNEUROSCI.1782-24.2025.
50. Wang, C., Chen, X., Lee, H., Deshmukh, S.S., Yoganarasimha, D., Savelli, F., and Knierim, J.J. (2018). Egocentric coding of external items in the lateral entorhinal cortex. Science *362*, 945–949. https://doi.org/10.1126/science.aau4940.
51. Gofman, X., Tocker, G., Weiss, S., Boccara, C.N., Lu, L., Moser, M.-B., Moser, E.I., Morris, G., and Derdikman, D. (2019). Dissociation between postrhinal cortex and downstream parahippocampal regions in the representation of egocentric boundaries. Curr. Biol. *29*, 2751–2757.e4. https://doi.org/10.1016/j.cub.2019.07.007.
52. Hinman, J.R., Chapman, G.W., and Hasselmo, M.E. (2019). Neuronal representation of environmental boundaries in egocentric coordinates. Nat. Commun. *10*, 2772. https://doi.org/10.1038/s41467-019-10722-y.
53. LaChance, P.A., Todd, T.P., and Taube, J.S. (2019). A sense of space in postrhinal cortex. Science *365*, eaax4192. https://doi.org/10.1126/science.aax4192.
54. Alexander, A.S., Robinson, J.C., Stern, C.E., and Hasselmo, M.E. (2023). Gated transformations from egocentric to allocentric reference frames involving retrosplenial cortex, entorhinal cortex, and hippocampus. Hippocampus *33*, 465–487. https://doi.org/10.1002/hipo.23513.
55. van Wijngaarden, J.B., Babl, S.S., and Ito, H.T. (2020). Entorhinal-retrosplenial circuits for allocentric-egocentric transformation of boundary coding. eLife *9*, e59816. https://doi.org/10.7554/eLife.59816.
56. Kunz, L., Brandt, A., Reinacher, P.C., Staresina, B.P., Reifenstein, E.T., Weidemann, C.T., Herweg, N.A., Patel, A., Tsitsiklis, M., Kempter, R., et al. (2021). A neural code for egocentric spatial maps in the human medial temporal lobe. Neuron *109*, 2781–2796.e10. https://doi.org/10.1016/j.neuron.2021.06.019.
57. Long, X., Deng, B., Cai, J., Chen, Z.S., and Zhang, S.-J. (2021). Egocentric asymmetric coding in sensory cortical border cells. Preprint at bioRxiv. https://doi.org/10.1101/2021.03.11.434952.
58. Mao, D., Avila, E., Caziot, B., Laurens, J., Dickman, J.D., and Angelaki, D.E. (2021). Spatial modulation of hippocampal activity in freely moving macaques. Neuron *109*, 3521–3534.e6. https://doi.org/10.1016/j.neuron.2021.09.032.
59. Luo, W., Yun, D., Hu, Y., Tian, M., Yang, J., Xu, Y., Tang, Y., Zhan, Y., Xie, H., and Guan, J.-S. (2022). Acquiring new memories in neocortex of hippocampal-lesioned mice. Nat. Commun. *13*, 1601. https://doi.org/10.1038/s41467-022-29208-5.
60. Ormond, J., and O'Keefe, J. (2022). Hippocampal place cells have goal-oriented vector fields during navigation. Nature *607*, 741–746. https://doi.org/10.1038/s41586-022-04913-9.
61. Campagner, D., Vale, R., Tan, Y.L., Iordanidou, P., Pavón Arocas, O., Claudi, F., Stempel, A.V., Keshavarzi, S., Petersen, R.S., Margrie, T.W., et al. (2023). A cortico-collicular circuit for orienting to shelter during escape. Nature *613*, 111–119. https://doi.org/10.1038/s41586-022-05553-9.
62. Martins, D.M., Manda, J.M., Goard, M.J., and Parker, P.R.L. (2024). Building egocentric models of local space from retinal input. Curr. Biol. *34*, R1185–R1202. https://doi.org/10.1016/j.cub.2024.10.057.
63. LaChance, P.A., and Hasselmo, M.E. (2024). Distinct codes for environment structure and symmetry in postrhinal and retrosplenial cortices. Nat. Commun. *15*, 8025. https://doi.org/10.1038/s41467-024-52315-4.
64. Lian, Y., LaChance, P.A., Malmberg, S., Hasselmo, M.E., and Burkitt, A.N. (2024). Distinct cortical spatial representations learned along disparate visual pathways. Preprint at bioRxiv. https://doi.org/10.1101/2024.10.10.617687.
65. Park, K., Yeo, Y., Shin, K., and Kwag, J. (2024). Egocentric neural representation of geometric vertex in the retrosplenial cortex. Nat. Commun. *15*, 7156. https://doi.org/10.1038/s41467-024-51391-w.
66. Zipser, D., and Andersen, R.A. (1988). A back-propagation programmed network that simulates response properties of a subset of posterior parietal neurons. Nature *331*, 679–684. https://doi.org/10.1038/331679a0.
67. Salinas, E., and Abbott, L.F. (1995). Transfer of coded information from sensory to motor networks. J. Neurosci. *15*, 6461–6474. https://doi.org/10.1523/JNEUROSCI.15-10-06461.1995.
68. Taube, J.S. (2007). The head direction signal: origins and sensory-motor integration. Annu. Rev. Neurosci. *30*, 181–207. https://doi.org/10.1146/annurev.neuro.29.051605.112854.
69. Angelaki, D.E., and Laurens, J. (2020). The head direction cell network: attractor dynamics, integration within the navigation system, and three-dimensional properties. Curr. Opin. Neurobiol. *60*, 136–144. https://doi.org/10.1016/j.conb.2019.12.002.
70. Giocomo, L.M., Stensola, T., Bonnevie, T., Van Cauter, T., Moser, M.-B., and Moser, E.I. (2014). Topography of head direction cells in medial entorhinal cortex. Curr. Biol. *24*, 252–262. https://doi.org/10.1016/j.cub.2013.12.002.
71. Jacob, P.-Y., Casali, G., Spieser, L., Page, H., Overington, D., and Jeffery, K. (2017). An independent, landmark-dominated head-direction signal in dysgranular retrosplenial cortex. Nat. Neurosci. *20*, 173–175. https://doi.org/10.1038/nn.4465.
72. Kornienko, O., Latuske, P., Bassler, M., Kohler, L., and Allen, K. (2018). Non-rhythmic head-direction cells in the parahippocampal region are not constrained by attractor network dynamics. eLife *7*, e35949. https://doi.org/10.7554/eLife.35949.
73. Zutshi, I., Fu, M.L., Lilascharoen, V., Leutgeb, J.K., Lim, B.K., and Leutgeb, S. (2018). Recurrent circuits within medial entorhinal cortex superficial layers support grid cell firing. Nat. Commun. *9*, 3701. https://doi.org/10.1038/s41467-018-06104-5.
74. Dudchenko, P.A., Wood, E.R., and Smith, A. (2019). A new perspective on the head direction cell system and spatial behavior. Neurosci. Biobehav. Rev. *105*, 24–33. https://doi.org/10.1016/j.neubiorev.2019.06.036.

75. Munn, R.G., and Giocomo, L.M. (2020). Multiple head direction signals within entorhinal cortex: origin and function. Curr. Opin. Neurobiol. *64*, 32–40. https://doi.org/10.1016/j.conb.2020.01.015.

76. LaChance, P.A., Graham, J., Shapiro, B.L., Morris, A.J., and Taube, J.S. (2022). Landmark-modulated directional coding in postrhinal cortex. Sci. Adv. *8*, eabg8404. https://doi.org/10.1126/sciadv.abg8404.

77. Yoganarasimha, D., Yu, X., and Knierim, J.J. (2006). Head direction cell representations maintain internal coherence during conflicting proximal and distal cue rotations: comparison with hippocampal place cells. J. Neurosci. *26*, 622–631. https://doi.org/10.1523/JNEUROSCI.3885-05.2006.

78. Taube, J.S., Stackman, R.W., Calton, J.L., and Oman, C.M. (2004). Rat head direction cell responses in zero-gravity parabolic flight. J. Neurophysiol. *92*, 2887–2997. https://doi.org/10.1152/jn.00887.2003.

79. Gibson, B., Butler, W.N., and Taube, J.S. (2013). The head-direction signal is critical for navigation requiring a cognitive map but not for learning a spatial habit. Curr. Biol. *23*, 1536–1540. https://doi.org/10.1016/j.cub.2013.06.030.

80. Taube, J.S., Wang, S.S., Kim, S.Y., and Frohardt, R.J. (2013). Updating of the spatial reference frame of head direction cells in response to locomotion in the vertical plane. J. Neurophysiol. *109*, 873–888. https://doi.org/10.1152/jn.00239.2012.

81. Page, H.J.I., Wilson, J.J., and Jeffery, K.J. (2018). A dual-axis rotation rule for updating the head direction cell reference frame during movement in three dimensions. J. Neurophysiol. *119*, 192–208. https://doi.org/10.1152/jn.00501.2017.

82. Ajabi, Z., Keinath, A.T., Wei, X.-X., and Brandon, M.P. (2023). Population dynamics of head-direction neurons during drift and reorientation. Nature *615*, 892–899. https://doi.org/10.1038/s41586-023-05813-2.

83. Stackman, R.W., Tullman, M.L., and Taube, J.S. (2000). Maintenance of rat head direction cell firing during locomotion in the vertical plane. J. Neurophysiol. *83*, 393–405. https://doi.org/10.1152/jn.2000.83.1.393.

84. Calton, J.L., and Taube, J.S. (2005). Degradation of head direction cell activity during inverted locomotion. J. Neurosci. *25*, 2420–2428. https://doi.org/10.1523/JNEUROSCI.3511-04.2005.

85. Jeffery, K.J., Anand, R.L., and Anderson, M.I. (2006). A role for terrain slope in orienting hippocampal place fields. Exp. Brain Res. *169*, 218–225. https://doi.org/10.1007/s00221-005-0138-3.

86. Moghaddam, M., Kaminsky, Y.L., Zahalka, A., and Bures, J. (1996). Vestibular navigation directed by the slope of terrain. Proc. Natl. Acad. Sci. USA *93*, 3439–3443. https://doi.org/10.1073/pnas.93.8.3439.

87. Miniaci, M.C., Scotto, P., and Bures, J. (1999). Place navigation in rats guided by a vestibular and kinesthetic orienting gradient. Behav. Neurosci. *113*, 1115–1126. https://doi.org/10.1037//0735-7044.113.6.1115.

88. Rigotti, M., Barak, O., Warden, M.R., Wang, X.-J., Daw, N.D., Miller, E.K., and Fusi, S. (2013). The importance of mixed selectivity in complex cognitive tasks. Nature *497*, 585–590. https://doi.org/10.1038/nature12160.

89. Fusi, S., Miller, E.K., and Rigotti, M. (2016). Why neurons mix: high dimensionality for higher cognition. Curr. Opin. Neurobiol. *37*, 66–74. https://doi.org/10.1016/j.conb.2016.01.010.

90. Hardcastle, K., Maheswaranathan, N., Ganguli, S., and Giocomo, L.M. (2017). A multiplexed, heterogeneous, and adaptive code for navigation in medial entorhinal cortex. Neuron *94*, 375–387.e7. https://doi.org/10.1016/j.neuron.2017.03.025.

91. Moore, J.J., Cushman, J.D., Acharya, L., Popeney, B., and Mehta, M.R. (2021). Linking hippocampal multiplexed tuning, Hebbian plasticity and navigation. Nature *599*, 442–448. https://doi.org/10.1038/s41586-021-03989-z.

92. Zhou, S., Seay, M., Taxidis, J., Golshani, P., and Buonomano, D.V. (2023). Multiplexing working memory and time in the trajectories of neural networks. Nat. Hum. Behav. *7*, 1170–1184. https://doi.org/10.1038/s41562-023-01592-y.

93. Mathis, A., Mamidanna, P., Cury, K.M., Abe, T., Murthy, V.N., Mathis, M.W., and Bethge, M. (2018). DeepLabCut: markerless pose estimation of user-defined body parts with deep learning. Nat. Neurosci. *21*, 1281–1289. https://doi.org/10.1038/s41593-018-0209-y.

94. Aronov, D., and Tank, D.W. (2014). Engagement of neural circuits underlying 2D spatial navigation in a rodent virtual reality system. Neuron *84*, 442–456. https://doi.org/10.1016/j.neuron.2014.08.042.

95. Zhou, P., Resendez, S.L., Rodriguez-Romaguera, J., Jimenez, J.C., Neufeld, S.Q., Giovannucci, A., Friedrich, J., Pnevmatikakis, E.A., Stuber, G.D., Hen, R., et al. (2018). Efficient and accurate extraction of in vivo calcium signals from microendoscopic video data. eLife *7*, e28728. https://doi.org/10.7554/eLife.28728.

96. Pnevmatikakis, E.A., and Giovannucci, A. (2017). NoRMCorre: An online algorithm for piecewise rigid motion correction of calcium imaging data. J. Neurosci. Methods *291*, 83–94. https://doi.org/10.1016/j.jneumeth.2017.07.031.

97. Sheintuch, L., Rubin, A., Brande-Eilat, N., Geva, N., Sadeh, N., Pinchasof, O., and Ziv, Y. (2017). Tracking the same neurons across multiple days in Ca2+ imaging data. Cell Rep. *21*, 1102–1115. https://doi.org/10.1016/j.celrep.2017.10.013.

98. Cai, D.J., Aharoni, D., Shuman, T., Shobe, J., Biane, J., Song, W., Wei, B., Veshkini, M., La-Vu, M., Lou, J., et al. (2016). A shared neural ensemble links distinct contextual memories encoded close in time. Nature *534*, 115–118. https://doi.org/10.1038/nature17955.

99. Vogelstein, J.T., Packer, A.M., Machado, T.A., Sippy, T., Babadi, B., Yuste, R., and Paninski, L. (2010). Fast nonnegative deconvolution for spike train inference from population calcium imaging. J. Neurophysiol. *104*, 3691–3704. https://doi.org/10.1152/jn.01073.2009.

STAR★METHODS

KEY RESOURCES TABLE

REAGENT or RESOURCE	SOURCE	IDENTIFIER
Bacterial and virus strains		
AAV2/9-hSyn-jGCaMP7s-WPRE-pA	Taitool	Cat#S0589-9
Chemicals, peptides, and recombinant proteins		
Dexamethasone	QUANYU Biological Technology Co.	Cat#163231147
Isoflurane	RWD	Cat#R510-22-10
Kwik-Sil	WPI Inc	N/A
Biological tissue glue	3M	Cat#1469SB
Dental acrylic	SND	Cat#19-7220
Phosphate-buffered saline	Gibco	Cat#10010500
Paraformaldehyde	Sigma-Aldrich	Cat#441244
O.C.T. compound	SAKURA	Cat#4583
DAPI-containing mounting medium	Solarbio	Cat#S2110
Sucrose	Aladdin	Cat#S112228
Deposited data		
Data and code	This study	https://github.com/XiaojingChenLab/GravityPPC
Experimental models: Organisms/strains		
C57BL/6J mice	Charles River	N/A
Software and algorithms		
Miniscope DAQ Software	Miniscope	https://github.com/daharoni/Miniscope_DAQ_Software
Miniscope DAQ QT Software	Miniscope	https://github.com/Aharoni-Lab/Miniscope-DAQ-QT-Software
GINKGO-MTPM	Transcend Vivoscope Biotech Co	N/A
DeepLabCut	Mathis et al.[93]	https://deeplabcut.github.io/DeepLabCut
Matlab	MathWorks	RRID: SCR_001622
ViRMEn	Aronov and Tank[94]	N/A
CNMF-E	Zhou et al.[95]	https://github.com/zhoupc/CNMF_E
NoRMCorre	Pnevmatikakis and Giovannucci[96]	https://github.com/flatironinstitute/NoRMCorre
CellReg	Sheintuch et al.[97]	https://github.com/zivlab/CellReg
Other		
Syringe	Hamilton	Cat#1701RN
GRIN lens	Edmund Optics	Cat#64519
Arduino Uno	ARDUINO	SKU A000066
AC servo motor	KIMBROUGH	110SY-M06030

EXPERIMENTAL MODEL AND SUBJECT DETAILS

Animals

Twelve male C57BL/6J mice (3–6 months old) were individually housed under a 12-hour light/dark cycle. Experiments were conducted during the dark phase. Throughout the experimental period, mice were subjected to water restriction to maintain approximately 90% of their pre-treatment body weight (with a minimum of 85%). All experiments and animal care adhered to the Laboratory Animal Use Protocol of the Southern University of Science and Technology Animal Care and Use Committee.

METHOD DETAILS

Surgical Procedures

Mice were placed in a closed induction chamber and anesthetized with a mixture of 2–3% isoflurane gas (O_2 flow rate: 0.5 L/min). Once deep anesthesia was achieved, mice were secured in a stereotaxic frame, and anesthesia was maintained with 1.5% isoflurane gas (O_2 flow rate: 0.5 L/min). A protective ointment was applied to the eyes. The skull was exposed, and a small hole was drilled to access the brain. A glass electrode was used to inject 500 nL of AAV2/9-hSyn-jGCaMP7s virus (1.0×10^{13} GC/mL, Taitool, China) into the right PPC (AP: -2.00 mm, ML: -1.70 mm, DV: 0.40 mm below the dura). The injection was performed slowly over 15 minutes, followed by a 15-minute waiting period before the electrode was removed. A 1.8 mm GRIN lens (Edmund Optics) was implanted at the injection site and secured using silicone adhesive (Kwik-Sil, WPI Inc, FL) to protect the area. A head plate was implanted to facilitate head fixation during the virtual reality task. After two weeks, a baseplate was attached to the lens. Following the surgery, mice were returned to their home cages and monitored to minimize stress during recovery.

Histology

After completing the experiments, mice were administered an overdose of sodium pentobarbital (1%, 150 mg/kg body weight, i.p.) to achieve deep anesthesia. Once anesthetized, mice were transcardially perfused with phosphate-buffered saline (PBS) to clear the blood, followed by perfusion fixation with 4% paraformaldehyde (PFA). The brain tissue was then carefully extracted and stored at 4°C for post-fixation. Subsequently, the brain was immersed in a 30% sucrose solution. Once the tissue sank to the bottom of the solution, it was embedded in O.C.T. compound (Tissue-Tek®) for cryosectioning. After embedding, the brain was coronally sectioned at a thickness of 40 μm using a cryostat microtome (Leica CM1950, Germany). The brain sections were then mounted on slides, and a DAPI-containing mounting medium was applied to seal the slides. Finally, bright field and fluorescence imaging (Tissue FAX Plus, TissueGnostics, Austria) were performed to identify the location of viral expression.

The horizontal open field foraging task

Mice used for behavioral tasks were water-restricted 3 days in advance. During this period, they were also accustomed to the experimenter for 15 minutes each day to minimize stress responses. Mice were then placed into a horizontal behavioral arena (square box: 60 cm × 60 cm × 50 cm). The arena had a white south wall and black walls on the other three sides, with an LED wall lamp mounted on the upper part of the north wall. Both the light source as well as the asymmetrical configuration of the behavioral arena (including the walls) provided salient visual polarizing cues to serve the visual reference frame. The room light was turned off, and the only other light source was a dim computer screen oriented away from the behavioral apparatus. Note that, the wall lamp was likely the primary light source for the animals (the computer screen is dimly lit, outside the mouse's field of view). The floor was made of 1-cm-thick styrofoam board. A camera was positioned directly above the arena to record the mouse's trajectory. The mice were trained and recorded under horizontal conditions. After approximately three days of training, recordings were conducted. To encourage exploration, water droplets were randomly dispensed to different locations in the arena as a reward. The frequency of water dispensing was gradually reduced once the mice exhibited sustained exploratory behavior. Each session lasted for ~30 minutes, with the total water volume not exceeding the daily limit (1 mL). One session was conducted per day. Mice were weighed before and after each experiment.

The sloping terrain task

The sloping terrain task was similar to the horizontal open field foraging task except that the arena was tilted in the former. To form a sloping terrain, the entire arena was tilted at three different angles (0°, 20°, and 40°). To ensure maximal distinction from the visual reference frame (north-south axis, as the LED lamp was on the north wall, and the south wall was white), the tilting operation was conducted along the east-west axis, with the default orientation being eastward, i.e., the west side of the box was raised (for example, 20°E is 20° tilted, the tilt orientation is eastward). The tracking camera angle was maintained parallel to the floor of the arena. There were three types of experiments in this task: the tilted experiment, the cue-conflict experiment and the dark experiment. Six PPC mice performed the former two experiments, two PPC mice performed the third experiment (Table S1).

The tilted experiment

The mice were trained under 0°, 20°E, and 40°E tilted conditions. The mice were first trained under the horizontal (0° tilted) condition. If the mice showed good behavioral performance, they proceeded with training under the 20°E and 40°E conditions, respectively. The entire training period lasted 5 to 8 days. Neural recordings were then conducted over three consecutive days, with one session per day at 0°, 20°E, and 40°E, respectively.

The cue-conflict experiment

For the cue-conflict experiment, we created the misalignment between two sets of cues: the visual cue (aligned with the north-south axis) and the gravity cue (aligned with the east-west axis).

Two tilt configurations were set at each tilt angle: westward tilt (e.g., 20°W), elevating the east side of the box caused the gravity vector to project westward; and eastward tilt (e.g., 20°E), elevating the west side projected the gravity vector eastward. This design created a 180°-mismatch between gravity signals while maintaining the visual cues. The camera frame of reference was always registered to the box-aligned visual reference frame.

Similar to the tilted experiment, mice were trained under 0°, 20°E, and 40°E tilt conditions. However, for the recording phase, mice underwent two recording sessions daily for three consecutive days, with an interval exceeding 30 minutes between sessions. The

recording protocol was as follows: Day 1: 0°, 40°E; Day 2: 20°W, 40°W; Day 3: 0°, 20°E. Note that 20°W and 40°W conditions were not trained prior to recording.

The dark experiment

To examine whether gravitational cues can serve as an independent reference frame for anchoring head-direction coding, we performed a control experiment in total darkness. An infrared camera was used to capture the movement of the animal in the dark. To capture the head direction of the animals in the dark, two motion-capture stickers of different sizes were mounted on the animals' heads. The stickers reflected more readily infrared light and thus could be used to track head direction.

Similar to the tilt experiment, animals were trained in the standard square box with standard lighting conditions for both 0° and 40° tilt configurations. During recording, the animals completed two sessions per day, one light session and one dark session. On day 1, the 0° tilt condition was used, whereas on day 2, the 40° tilt condition was used. Each session lasted 20 min, with more than 30 min intervals between two recording sessions. Note that, during the Dark session, all the light sources of the whole behavioral room were turned off.

The tilted virtual reality task

The tilted virtual reality (VR) task is a linear track navigation paradigm[38] controlled by a custom ViRMEn-based software and hardware system.[94] Mice were head-fixed on a styrofoam running wheel (6 cm width, 7.5 cm radius), and the visual environment was presented through three seamlessly integrated 24-inch displays at an angle of 150°, simulating a linear track. The wheel axis was connected to a rotary encoder, which captured the movement of the mice. This movement data was processed by a microcontroller (custom PCB + Arduino Mega 2560) and relayed in real-time to a host computer that updated the VR environment, forming a closed-loop control system. At the end of each track, a lick port delivered a water reward (25 μL) controlled by a peristaltic pump. Both running and licking data were continuously monitored and transmitted to the host computer for analysis. All components were mounted on an adjustable platform capable of tilting to specific angles. In this experiment, the tilted VR task was conducted under two conditions: 0° (flat) and 40° tilt (left side elevated).

Standard Experiment

The standard VR world consisted of a 200 cm linear track, with four landmarks evenly spaced at 25 cm (left), 75 cm (right), 125 cm (left), and 175 cm (right). The linear track was repeated seamlessly to create an infinite environment without intervals. Completion of one full track was defined as a lap.

As in the open-field experiments, mice were water-restricted. They were first acclimated to the VR system before beginning the formal experiments, which comprised a training phase and a recording phase. During the training phase, each session lasted 20 minutes, with two sessions per day (one at 0° tilt and one another at 40° tilt, presented in random order) separated by at least 30 minutes. Training was conducted for 3–5 days. In the recording phase, a Miniscope was mounted onto the baseplate to capture neuronal activity in the target brain area.

Direction-reversal Experiment

The direction-reversal world was a modified version of the standard world. Landmarks were placed at 25 cm (left), 75 cm (left), 125 cm (left), and 175 cm (right), with the second landmark shifted from the right to the left side. Unlike the standard experiment protocol, this experiment required mice to perform alternating forward and reverse running directions on a lap-by-lap basis within the visual environment.

Data collection

In this study, 12 mice were used, including 11 PPC mice and a RSC mouse. Five mice performed both the open-field task and the virtual reality task, six mice performed only the open-field task, and one mouse performed only the virtual reality task. (Table S1: For the open-field task, data for the horizontal experiment were collected from 8 mice, while data for the tilted experiment and cue conflict experiment were collected from 6 mice, data for dark experiment were collected from 2 mice. For the VR task, data for the standard experiment were collected from 4 mice, while data for the direction-reversal experiment were collected from 6 mice.)

All 12 mice were used for one-photon recording. The calcium fluorescence signal was acquired at 15 Hz using Miniscope[98] (an open-source micro-endoscope hardware and software suite: miniscope.org, version 3).

The methods of behavioral data acquisition differed depending on the specific task. For the open-field task, two LEDs (red on the left and green on the right) were attached to the scope body to indicate the position and head direction of the mice. The behavioral data were acquired at 20 Hz. For the virtual reality task, the position of the mice in the VR world was recorded at 30 Hz.

QUANTIFICATION AND STATISTICAL ANALYSIS

Statistical analyses were conducted using MATLAB (MathWorks). The primary statistical methods included Cochran-Armitage trend test, Fisher's exact test, Chi-squared test, Kruskal-Wallis test combined with Dunn's test for multiple comparisons (Dunn-Sidak correction), Wilcoxon rank-sum test, Wilcoxon signed-rank test, Friedman test, Rayleigh test, and Kolmogorov-Smirnov test, applied as appropriate. The statistical details, including the tests used, the statistics, the exact value of n, what n represents, and measures of central tendency (e.g., mean or median), are reported in the results section and the legends of Figures S1–S7. Significance levels in Figures are indicated using asterisks: * for $p < 0.05$, ** for $p < 0.01$, and *** for $p < 0.001$.

Behavioral variables and neuronal signal extraction

Behavioral trajectory in 2-dimensional tasks

The detailed method can be found in a previous study.[38] Briefly, in the open-field experiment, the positions of the two-color LEDs on the head-mounted micro-endoscope were used to measure the head position and head direction (LEDs were replaced by motion-capture stickers in dark sessions). First, the positions of the two LEDs in the behavioral video were extracted using DeepLabCut method.[93] The extracted video position signals were then smoothed using a zero-phase filter with a 250 ms (5 frames) window. The video position signals were remapped to the standard-sized square open-field coordinates (with the center of the open field as the origin).

Head direction and egocentric boundary bearing

Based on the positional relationship between the red LED and the green LED, the mouse's head orientation can be determined. The angle between the head orientation and the positive direction of the X-axis (south) is defined as the head direction, where 0°, 90°, 180°, and 270° represent south, east, north, and west, respectively.

The egocentric bearing of the nearest boundary is defined as the angle between the vector pointing from the nearest boundary coordinate to the mouse's position coordinate and the unit vector representing the mouse's head direction.[38,50] Given the constant geometric relationship between the egocentric bearing of the nearest boundary and that of the center point, they are treated as equivalent in this study. Angles of 0°, 90°, 180°, and 270° represent the nearest boundary being located at the front, left, rear, and right of the mouse, respectively.

Both the head direction signal and the egocentric boundary signal were smoothed using a circular filter with a 250 ms (5-frame) window.

Position in the virtual reality

The positional signals of the mice in the VR environment were extracted from the ViRMEn system.

Neuron Segmentation and Calcium Signal Extraction

Raw single-photon calcium imaging videos were first subjected to segmented rigid motion correction to eliminate motion artifacts.[96] The Constrained Nonnegative Matrix Factorization for microendoscopic data (CNMF-E) approach was then applied to separate the background, extract neuron positions and contours, and obtain calcium activity time series.[95] Next, the calcium activity time series of all neurons was processed using the fast OOPSI algorithm to perform detrending and deconvolution, estimating the spike trains underlying the observed calcium activity.[99] The inferred spike trains were termed the calcium event. These calcium event time series were used for subsequent data analysis.

A cell registration method was employed to align cell identities across different sessions, which modeled the distribution of similarities between neighboring cells across sessions.[97] This alignment was used to analyze the coding properties of the same cells across sessions or days. Note that, during the process of the cell registration across sessions, some cells could not be tracked with confidence (due to change of focal plane or movements of the brain, etc.). This didn't imply these cells turned on or off across sessions.

For all datasets, only data from periods when the mice's movement speed exceeded 3 cm/s were included in subsequent analyses.

Data analysis

Allocentric head direction tuning

To identify head direction cells, we first constructed the head direction tuning curve for each neuron. The head direction was divided into 18 bins, ranging from 0° to 360°, with each bin spanning 20°. The firing rate in each bin was calculated as the total response of calcium events divided by the time spent in the respective bin. The strength of directional selectivity in head direction tuning was quantified using the Mean Vector Length (MVL),[38] which ranges from 0 to 1:

$$MVL = \frac{\left| \sum_{k=1}^{n} r_k \cdot e^{i \cdot \theta_k} \right|}{\sum_{k=1}^{n} r_k}$$

where n is the number of head direction bins, r_k is the firing rate (amplitude) for the k-th sample, and θ_k is the corresponding angle (head direction). A higher MVL indicates a stronger directional coding by the neuron.

A neuron was classified as a head direction cell if it met all the following criteria: 1) Only active neurons were included in the analysis (total calcium events > 30); 2) The MVL value exceeded 95th percentile of the null distribution generated by the shuffling procedure. 3) The MVL value exceeded 0.25.

Definition of G-cell and V-cell in the cue-conflict experiment

To investigate the reference frame selection of head direction cells (HDCs) under tilt conditions, we defined two types of HDCs based on their alignment with external cues (gravity or vision). Only cells classified as HDCs (at least in one session) were included in this analysis: G-cell (gravity-anchored HDC), defined as cells whose absolute shift of preferred firing direction (PFD) between opposite tilt conditions fell within the range [135°, 180°], i.e., switch to the opposite direction; and V-cell (vision-anchored HDC), defined as cells whose absolute shift of PFD between opposite tilt conditions fell within the range [0°, 45°], i.e., kept their PFD. In the horizontal condition where gravitational reference is unavailable, HDCs were automatically categorized as vision-anchored (V-cells).

Egocentric boundary bearing tuning

The method for determining egocentric boundary cells and their preferred direction follows the same procedure as that used for head direction cells described above. Specifically, the firing rate of each cell is calculated for different angular bins, and these rates are weighted by the corresponding angular values to obtain a complex vector representation. The optimal direction is then determined by calculating the weighted average direction, considering the firing rates as the weights. The directionality score is quantified by the modulus of the sum of the complex vectors, normalized by the total firing rate, reflecting the strength of the cell's directional encoding. The preferred direction is computed by determining the phase angle of the complex vector sum, ensuring the result lies within the range [0, 2π] through modulo operation.

Construction of egocentric boundary ratemaps (EBRs)

EBRs are 2D spatial-like ratemaps referenced relative to the animal, which depict the neuron's angle and distance preference for boundaries.[37,38,51,52] The egocentric space was binned in a polar coordinate, with 120 angular bins (bin size: 3°) and 15 distance bins (bin size: 2 cm). For each video frame, the boundaries that fall into the egocentric space (120×15 bins) will be counted into the corresponding bins. For each neuron, the firing rate of each 3°×2 cm bin was calculated by dividing the calcium fluorescence signal in the given bin by the time that the animal spent in that bin. The EBRs were smoothed by a Gaussian filter (3 bin width, one bin SD).

Distance preference and distance selectivity index (DSI)

For the EBC, we also analyzed their distance preferences. Two methods were used. First, the distance of the peak firing rate on the PFD of EBRs. Second, the distance of the peak firing rate on the distance tuning curve.

We also defined a distance selectivity index to quantify the distance selectivity of EBCs:

$$DSI = \frac{R_{max} - R_{min}}{R_{max} + R_{min}}$$

where R_{max} is the maximum firing rate of the distance tuning curve; R_{min} is the minimum firing rate of the distance tuning curve. The range of DSI is between 0 and 1. The larger the DSI, the more distance-selective the cell is.

Shuffling procedures

Calcium events were temporally shifted by a random amount, with the shift distance ranging from 20% to 80% of the total duration. After each shift, the mean vector length (MVL) or other measures were recalculated. This shuffling procedure was repeated 1000 times to generate distributions of MVL values (for the open-field task) and landmark score values (for the VR task, see below) under the null hypothesis.

Egocentric landmark cell analysis

The detailed method can be found in a previous study.[38] Specifically, to determine the egocentric landmark bearing tuning of neurons, the distance from 0 to 200 cm was divided into 40 bins, each 5 cm wide. The firing rate for each bin was calculated, generating the neuronal tuning curve along the track. This curve was then smoothed using a Gaussian filter (filter size: 5 bins, sigma: 3 bins) for circular smoothing and subsequently normalized.

To identify egocentric landmark cells, we applied a template-matching method to calculate the egocentric landmark score. First, we constructed an egocentric landmark tuning template (ground truth). In the case of a standard world, the template is composed of two fields, with the centers of these fields spaced 20 bins apart (i.e., 100 cm). Depending on the position of the field centers, 21 distinct tuning templates are generated. By computing the Pearson correlation between the neuronal tuning curve and each of the templates, we identified the template with the highest correlation. The local correlation within 6 bins (30 cm) around the field center was then calculated, and the average correlation between the template and the neuronal tuning curve in this region was defined as the egocentric landmark score.

The criteria for identifying an egocentric landmark cell include the following: 1) The neuron is an active cell (the number of calcium events > 30); 2) The landmark score exceeds the 95th percentile of the null distribution generated by the shuffling procedure. 3) The landmark score is greater than 0.5.

Allocentric landmark cell analysis

Similar to egocentric landmark cells, to identify allocentric landmark cells, the template-matching method was used to calculate the allocentric landmark score. The template is composed of four fields, with the centers of these fields spaced 10 bins apart (i.e., 50 cm). Depending on the position of the field centers, 11 distinct tuning templates are generated. By computing the Pearson correlation between the neuronal tuning curve and each of the templates, we identified the template with the highest correlation. The local correlation within 6 bins (30 cm) around the field center was then calculated, and the average correlation between the template and the neuronal tuning curve in this region was defined as the allocentric landmark score.

The criteria for identifying an allocentric landmark cell include the following: 1) The neuron is an active cell (the number of calcium events > 30); 2) The landmark score exceeds the 95th percentile of the null distribution generated by the shuffling procedure. 3) The landmark score is greater than 0.5.

Construction of egocentric landmark rate maps (ELRs)

The ELRs were similar to EBRs, 2D spatial-like rate maps referenced relative to the animal, which depict the neuron's angle and distance preference for landmarks. The egocentric space was binned in a polar coordinate, with 360 angular bins (bin size: 1°) and 25 distance bins (bin size: 4 cm). Each landmark occupies a local zone with a 5 cm radius. There are multiple firing fields in this map, as there are multiple landmarks in the environment.

Egocentric index (EI)

For the landmark cells in VR tasks, we defined an egocentric index based on the ELRs to quantify the egocentric reference preference:

$$EI = \frac{R_{peak} - R_{mirror}}{R_{peak} + R_{mirror}}$$

where R_{peak} is the peak firing rate of ELR, the corresponding angle-distance bin is Bin_{peak}; Bin_{mirror} is the contralateral angle-distance bin of Bin_{peak}. R_{mirror} is the firing rate in Bin_{mirror}. The range of EI is between 0 and 1. This index measures how asymmetric the firing is at the peak. Higher EI values indicate egocentric properties, whereas lower values indicate more allocentric properties.

Difference of Preferred Firing Direction (PFD) between sessions

To evaluate the change of PFD between different recording sessions, the angular shift of PFD was calculated ($\Delta PFD = PFD_{s2} - PFD_{s1}$). It ranges from -180° to 180°.

Additionally, we also defined another type (ΔPFD) based on the cross-correlation analysis of tuning curves between different sessions for additional analytical insights, which is defined as the angular lag when the maximum cross-correlation occurs (CC^{max}). This metric was used to identify the reference frame selection among HDCs under opposite tilt configurations.

Change of Preferred Firing Direction (PFD) between sessions

To investigate the change of PFD between reference frames (especially from V-cell to G-cells) between manipulations, we isolated HDC that switched from V-cell to G-cell. We calculated the difference between the PFD in the first session (PFD_V) and the PFD in the second session ($PFD_{G\text{-}E}$ or $PFD_{G\text{-}W}$, which were the PFD for eastward and westward tilt conditions). As these cells were identified as G-cells in the second session, the $PFD_{G\text{-}W}$ and $PFD_{G\text{-}E}$ usually differed by 180° (see the definition above):

$$\Delta 1 = PFD_V - PFD_{G-E}$$

$$\Delta 2 = PFD_V - PFD_{G-W}$$

We selected the angle change (Δ) with the smaller absolute magnitude for each cell:

$$\Delta_{selected} = \begin{cases} \Delta_1, if\ |\Delta_1| \leq |\Delta_2| \\ \Delta_2, otherwise \end{cases}$$

We then analyzed the distribution of the selected delta angles ($\Delta_{selected}$).